# Demonstrating a superconducting dual-rail cavity qubit with erasure-detected logical measurements

Kevin S. Chou,[1,*] Tali Shemma,[1] Heather McCarrick,[1] Tzu-Chiao Chien,[1] James D. Teoh,[2,3] Patrick Winkel,[2,3] Amos Anderson,[1] Jonathan Chen,[1] Jacob Curtis,[2,3] Stijn J. de Graaf,[2,3] John W. O. Garmon,[2,3] Benjamin Gudlewski,[1] William D. Kalfus,[2,3] Trevor Keen,[1] Nishaad Khedkar,[1] Chan U Lei,[1] Gangqiang Liu,[1] Pinlei Lu,[1] Yao Lu,[2,3] Aniket Maiti,[2,3] Luke Mastalli-Kelly,[1] Nitish Mehta,[1] Shantanu O. Mundhada,[1] Anirudh Narla,[1] Taewan Noh,[1] Takahiro Tsunoda,[2,3] Sophia H. Xue,[2,3] Joseph O. Yuan,[1] Luigi Frunzio,[2,3] José Aumentado,[1,4] Shruti Puri,[2,3] Steven M. Girvin,[2,3] S. Harvey Moseley, Jr.,[1] and Robert J. Schoelkopf[1,2,3,†]

[1] *Quantum Circuits, Inc., 25 Science Park, New Haven, CT 06511, USA*
[2] *Departments of Applied Physics and Physics, Yale University, New Haven, Connecticut 06511, USA*
[3] *Yale Quantum Institute, Yale University, New Haven, Connecticut 06520, USA*
[4] *National Institute of Standards and Technology, Boulder, Colorado 80305, USA*



A critical challenge in developing scalable error-corrected quantum systems is the accumulation of errors while performing operations and measurements. One promising approach is to design a system where errors can be detected and converted into erasures. A recent proposal aims to do this using a dual-rail encoding with superconducting cavities. In this work, we implement such a dual-rail cavity qubit and use it to demonstrate a projective logical measurement with erasure detection. We measure logical state preparation and measurement errors at the 0.01%-level and detect over 99% of cavity decay events as erasures. We use the precision of this new measurement protocol to distinguish different types of errors in this system, finding that while decay errors occur with probability ∼0.2% per microsecond, phase errors occur 6 times less frequently and bit flips occur at least 170 times less frequently. These findings represent the first confirmation of the expected error hierarchy necessary to concatenate dual-rail erasure qubits into a highly efficient erasure code.

Practical quantum error correction requires achieving error rates well below threshold in the physical qubits during all operations. Most platforms still require substantial improvements in fidelity of not just gates but all operations, including state preparation and measurement. In addition to the quest for better physical qubits with lower error rates and fewer error channels, various avenues are being investigated to address these challenges. One approach is to implement error correction using qudits or multi-level bosonic modes to provide the necessary redundancy within a single physical element [1–5], and is the only architecture to have achieved breakeven for the lifetime of a logical qubit [6–9]. Alternatively, the correction thresholds can be less demanding if one can tailor codes [10–14] to exploit a natural or engineered structure or noise bias in the qubits [15–19]. While on the path to error correction, there are benefits in detecting errors as they occur in the physical qubits through the use of dedicated flag qubits [20–24].

The concept of erasure qubits extends error-detection to full error correction when incorporated in a higher-level stabilizer code. Erasure errors are defined as detected errors that occur at a specific time and location in the physical qubits [25]. A relatively new approach [26] is to build in the ability to appropriately detect [27–29] the dominant errors directly into the physical system, thereby converting them to erasures. It is known that any stabilizer code can correct for twice as many erasure errors compared to Pauli errors [25]. Additionally, large-scale error correction codes benefit from a higher threshold for erasure errors [26, 30, 31].

A simple way to realize an erasure qubit is with the dual-rail encoding, defined by the codewords $|0_L\rangle = |01\rangle$ and $|1_L\rangle = |10\rangle$ (see Fig. 1a). The encoding of this qubit in two spatial modes [32] or polarizations of an optical photon [33] is a well-known concept [34] that has been widely explored in linear optics platforms, and remains an active area of research [35]. The recently proposed circuit quantum electrodynamics (cQED) implementation of the dual-rail cavity qubit [36] has the distinct advantage of strong and controllable non-linearity via a dispersively coupled transmon ancilla, which enables on-demand arbitrary state preparation, entangling gates, and measurements enabled by efficient single-photon detection. Another approach to build erasure qubits out of transmon qubits [27] themselves has also been proposed. The bosonic cQED realization uses two microwave cavities, and offers the prospect of converting not only cavity photon loss, but also dominant ancilla errors [37–39], into detectable erasures. This can be achieved for a full set of single and two-qubit gates, as well as state preparation and measurement. A key design principle of the dual-rail cavity qubit is to engineer a system that exhibits a strong hierarchy of errors, with remaining Pauli and leakage error rates orders of magnitude smaller than erasure rates, resulting in a qubit optimized for integration into a higher-level error correction code. Already, recent work has demonstrated single-qubit operation fidelities for a dual-rail cavity qubit in excess of 99.95% [40, 41]. However, to fully exploit the benefits of this encoding, several

* chou@quantumcircuits.com
† robert.schoelkopf@yale.edu

other aspects are required.

In this work, we implement logical state preparation and measurement (SPAM) in a dual-rail cavity qubit. We design our logical measurement to have built-in erasure detection, rendering it insensitive to any single occurrence of the dominant hardware errors, including those arising from decoherence, initialization, and readout. The type of logical measurement we show is an example of end-of-the-line erasure detection, which finds use when measuring qubits at the end of an algorithm or when measuring error syndromes in a stabilizer circuit. This is in contrast with mid-circuit erasure detection, which preserves the logical information within the codespace when an erasure is not detected. Such a mid-circuit measurement is necessary for erasure conversion or correction, and is possible [42] with a different technique [36] within the same architecture. With our end-of-the-line measurement, we obtain SPAM errors that are among the lowest for any physical qubit platform, with logical errors at the 0.01% level. Additionally, we show that over 99% of decay errors can be detected as end-of-the-line erasures. We use this logical measurement to probe idling bit-flip and dephasing error rates in a dual-rail qubit, finding they are smaller than the measured erasure rates. Specifically, for this system we measure a cavity decay rate $\sim 0.2\%$ per microsecond, with phase and bit-flip errors measured to be a factor of 6 times and at least 170 times less likely, respectively. The development of a logical measurement with precise erasure detection is a key step for the dual-rail cavity qubit approach and enables detailed characterization of both erasures and the underlying small errors.

## RESULTS

### Characterizing dual-rail SPAM

We first describe the principle of measurement for the dual-rail cavity qubit. Logical measurement of a dual-rail cavity qubit detects which cavity, if any, contains the photon. In contrast to conventional qubit measurements, where performance is limited by misassignment and transition errors during the readout [45, 46], the logical measurement has the additional capability of labeling most of these readout errors and also cavity leakage errors as erasures. The logical measurement is expected to have both low logical misassignment errors and be a highly sensitive detector of leakage due to decay errors (photon loss), while ideally incurring only a small penalty from additional erasures due to readout errors. These properties are essential for a good dual-rail cavity qubit.

We describe our protocols for state preparation and measurement in the dual-rail encoding (see Materials and Methods for full detail). In our hardware implementation, each cavity has an individual ancilla transmon and readout for control and measurement (Fig. 1b), which allows simultaneous measurement of both cavities. As shown in Fig. 1c, the state preparation protocol consists of three steps: reset to $|00\rangle$, initialization in a logical state, and optional "check" measurements to verify the state preparation, which boosts the preparation fidelity. There are many options for the state preparation protocol. Here, we use an optimal control pulse (OCP) [47] to initialize a cavity in $|1\rangle$ and a single transmon measurement after the OCP to check that the transmon is in $|g\rangle$, as intended. Importantly for our SPAM protocol, any errors in the state preparation not caught by the check measurements can still be detected later in the logical measurement as an erasure, resulting in a slight increase in the erasure rate, but need not impact the fidelity of the logical outcome.

In our experiment, the logical measurement is implemented by performing simultaneous cavity measurements. For each cavity, we first perform a photon-number selective $\pi$-pulse to map the state of the cavity onto the transmon, flipping the transmon to $|e\rangle$ only if the cavity is in $|1\rangle$. This is followed by a standard dispersive readout of the transmon, with a total duration of 4.8 $\mu$s for the cavity measurement. There are many options for implementing the logical measurement and our chosen mapping operation is optimized for detection of the dominant leakage state, $|00\rangle$ (see Materials and Methods for more detail). Importantly, these photon-number-resolving measurements are non-demolition on the cavity photon number [46, 48] and as such the cavity measurements may be repeated to form multiple rounds of measurements, further suppressing assignment errors. In the case of multiple rounds of measurement, after each round of cavity measurements we reset both transmons to $|g\rangle$ by applying a conditional $\pi$-pulse if either transmon was found in $|e\rangle$. The reset is followed by an additional check to verify the transmons are in the ground state and assign any failures as an erasure. Finally, prior to the first logical measurement, we also perform transmon readouts to verify that both are in the ground state, also assigning failures as an erasure.

Each measurement round is decoded and assigned to one of four possible outcomes: codespace outcomes {"01", "10"} or erasure outcomes {"00", "11"}. In the case of repeated rounds of measurements disagreeing, we declare an ambiguous outcome "A". Given our mapping choice, each cavity measurement informs us whether or not the cavity is in $|1\rangle$. Higher leakage states in an individual cavity, such as $|2\rangle$, while less likely, are nonetheless assigned to outcome "0". As such, dual-rail cavity qubit leakage states, such as $|02\rangle$ or $|20\rangle$, will be assigned to "00" and labeled as an erasure. Finally, we discard the assigned erasures and compute the logical outcome $1_\mathrm{L}$ ($0_\mathrm{L}$), defined as $P_{1_\mathrm{L}\ (0_\mathrm{L})} = N_{1_\mathrm{L}\ (0_\mathrm{L})}/\left(N_{0_\mathrm{L}} + N_{1_\mathrm{L}}\right)$, where $N$ is the number of shots of the assigned logical state.

First, we perform our SPAM experiment by preparing logical states $|0_\mathrm{L}\rangle = |01\rangle$ and $|1_\mathrm{L}\rangle = |10\rangle$ and then performing a logical measurement. From the logical state preparation we can extract two figures of merit. First, the logical misassignment error is defined as the fraction of counts assigned to "10" ("01") when preparing

$|01\rangle$ ($|10\rangle$), this is represented by the assignment channel shown as pink arrows in Fig. 2a. From our data, shown as pink bars in Fig. 2b, we determine the logical misassignment error to be $(1.7 \pm 0.3) \times 10^{-4}$, averaged over both state preparations, or 17 counts out of a total of $10^5$. Second, we can quantify the erasure fraction as the relative number of counts labeled "00" or "11" (channel shown in blue arrows in Fig. 2a), which we measure to be $(5.62 \pm 0.05) \times 10^{-2}$, shown as blue bars in Fig. 2b. In addition to preparation errors, which constitute a leakage error, these assigned erasures can also arise from any single error during the dual-rail measurement, including leakage in a cavity, transmon decoherence, or readout errors. False erasure assignments, for which the dual-rail cavity qubit is still in the codespace, are false positives and set a lower bound on the erasure fraction.

By intentionally preparing leakage states $|00\rangle$ and $|11\rangle$, we directly test the erasure detection capability of our logical measurement. This assignment channel is shown with yellow arrows in Fig. 2a and the experimental results are shown in the right two panels in Fig. 2b. The critical figure of merit is what we call the leakage detection error, which is the fraction of false negatives, i.e. when we fail to detect a leakage event. Because undetected leakage errors are amongst the most damaging errors in a stabilizer code, it is important to keep the fraction of leaked qubits small [49–52]. We show that we can achieve this in our system by measuring the leakage detection error to be $(7.7 \pm 0.28) \times 10^{-3}$ when preparing $|00\rangle$, by far the dominant leakage due to photon loss. This means that we can convert $> 99\%$ of leakage errors during the measurement to erasures. The leakage detection error when preparing $|11\rangle$ is higher, at the $10^{-2}$ level but leakage to this state is much rarer, requiring a cavity heating event.

We have developed a detailed model to simulate the state preparation and measurement protocol (Supplementary Text), finding close agreement between these simulations (plotted as green lines in Fig. 2b) and our experimental data. Further, we have developed a simplified error model (Supplementary Text) to determine the physical error mechanisms that contribute to incorrectly assigned outcomes. Using this model, we infer that outcomes assigned as erasures are often transmon $T_1$ events during readout, contributing between 30%-50% of the total error. Leakage detection errors are dominated by readout classification errors, contributing between 60%-90% of the total error.

Finally, by performing the SPAM experiment with two rounds of measurements we observe an exceedingly low logical misassignment error of $(3 \pm 1) \times 10^{-5}$ and leakage detection errors of $(1.3 \pm 0.1) \times 10^{-3}$. We attribute this $\sim 6\times$ improvement to the decoding strategy where we require agreement between both rounds of measurements (see detailed breakdown of the error budget in Supplementary Materials). The tradeoff with this strategy is a much higher erasure fraction at $(18 \pm 1)\%$, which is well-accounted for in our model. This experiment highlights the flexibility of our measurement protocol, with options for both multiple rounds of measurements and strategies both for reduced SPAM error or for reduced erasures.

### Measuring bit-flip Error Rates

Having demonstrated a high-fidelity logical measurement, we now use this tool to probe idling errors in our dual-rail qubit. First, we study the dual-rail bit-flip error rate, defined here as the rate of transition from one logical state to the other: $|01\rangle \rightarrow |10\rangle$ and vice versa. We expect these transitions to be exceedingly rare, caused by a double error via photon-loss in one cavity and photon-gain in the other cavity, thereby inducing a bit-flip in the logical state. In our system, the cavities have relaxation times of $T_1 = 1/\kappa = 350$ $\mu$s and 592 $\mu$s and thermal populations of $n_{\text{th}} = 1.7 \times 10^{-4}$ and $3.5 \times 10^{-4}$ (see Materials and Methods). In this experiment, the qubit is prepared in either of the logical states $|01\rangle$ or $|10\rangle$ and a logical measurement is performed after a variable delay; the results are shown in Fig. 3a. At zero delay, the assigned outcomes are consistent with the $|01\rangle$ and $|10\rangle$ SPAM results, and we find the probability of assigning the bit-flip outcome to be $\sim 10^{-4}$. As the delay increases, we observe the expected exponential increase in the $|00\rangle$ population. At longer delay times, the assigned outcomes tend toward the measurement outcomes when preparing $|00\rangle$ as shown in our SPAM experiment. Our apparent bit-flip rate will have contributions both from the intrinsic bit-flip error rate, defined as the logical transition rate in the absence of measurement errors, and from measurement errors. We compare our data with two simulations, one with measured hardware parameters and the other with no intrinsic bit-flip errors by setting the cavity thermal populations $n_{\text{th}} = 0$ (see Fig. 3). We find both simulations largely agree with the measurement, suggesting that the bit-flip outcome counts are not dominated by actual state transitions in the cavities, but rather by measurement errors.

From the assigned physical outcomes we plot the logical bit-flip outcomes, shown in Fig. 3b. Given the high-fidelity logical measurement, we also perform these experiments at short times (20 $\mu s$) in order to directly observe idling errors on the few microsecond scale, the relevant timescale for a logical entangling gate [53]. We perform a linear fit to the short-time data, and show that the probability of apparent logical errors grows on the order of 0.001% in 1 $\mu$s, corresponding to a rate slower than 1/(79±24 ms). Our model suggests this rate is a lower bound for the intrinsic dual-rail bit-flip rate, as the intrinsic bit-flip contributes only $\sim 0.5\%$ of the apparent bit-flip even at 20 $\mu$s (Supplementary Text). Given the good agreement with the simulation, we infer that the intrinsic bit-flip rate should be non-exponential [36] and extremely slow, with a probability $\sim n_{th}(\kappa t)^2$ at short times, that would be only a few parts per billion in a microsecond (see Supplementary Text for details).

### Measuring dephasing rates

We perform Ramsey and echo experiments on the dual-rail cavity qubit to make a first estimate of phase errors. After state preparation in a logical dual-rail state, the Ramsey sequence is performed by applying a logical $\pi/2$-pulse, implemented via a parametric beamsplitter interaction [40, 41], and, after a variable delay, applying a second logical $\pi/2$-pulse, before measuring the qubit. In the case of the echo measurement, an additional logical $\pi$-pulse is inserted mid-way during the delay. For the Ramsey experiment, the beamsplitter is intentionally detuned by a small (5 kHz) amount, giving rise to periodic behavior of the superposition of states.

We present results for an initial estimate of the dephasing rates for our dual-rail qubit, as shown in Fig. 4. We compare our data to a simulation of the Ramsey and echo experiment, and infer dual-rail dephasing times by matching the data (or envelope of the data in the case for Ramsey) with our simulation. From this, we extract $T_\varphi = 1.76$ ms from the Ramsey experiment, and $T_\varphi^{\mathrm{E}} = 3.08$ ms from the echo experiment. In our data we observe an offset in $\langle Z_{\mathrm{L}} \rangle$ at long times, where it is expected to decay to zero. This can be explained by leakage detection errors that bias the logical measurement at long times, due to the increased probability of being in the $|00\rangle$ state. As such, we also perform coherence experiments at shorter times ($< 100\mu$s), where this bias is suppressed by the smaller probability of being in $|00\rangle$. From these experiments we extract dephasing error rates for Ramsey and echo of $(0.059 \pm 0.006)\%$ and $(0.037 \pm 0.003)\%$ per microsecond, respectively. From this we infer rates $1/(1.70{\pm}0.18$ ms) and $1/(2.70{\pm}0.20$ ms), respectively for Ramsey and echo, which is similar to our simulation results. The dual-rail $T_\varphi$ values are likely still dominated by extrinsic sources of cavity dephasing, introduced by finite heating rates and state transitions of the dispersively coupled nonlinear elements, which in our system are two measurement transmons and three Josephson coupling elements (see Fig. 1b). This initial bound on phase-flip rate measured here is encouraging, and is approximately a factor of six slower than the erasure rate. Further improvements are achievable, for example, by decreasing the heating rates in these elements and detecting their residual state transitions as erasures.

## CONCLUSION

We have developed a logical measurement with built-in erasure detection with logical misasssignment on the order of $10^{-4}$ and with efficiency for detecting leakage to $|00\rangle$ in excess of 99%. Our measurements show that the logical bit-flip rate is a factor of 170 smaller than the erasure rate, and that the logical phase-flip rate is a factor of 6 smaller, providing initial confirmation that dual-rail cavity qubits can have a favorable hierarchy of errors in the idling state. Further improvements in the measurement and characterization of dual-rail qubits should also be possible. While we have already demonstrated low error rates, a more detailed analysis (51) of the physical phenomena and the ultimate limits on dephasing in the dual-rail qubit are key questions. The erasures induced by measurement errors impact the post-selected yield in this experiment and further reduction in both real and apparent erasures will be beneficial. Fortunately, our modeling projects that improvements from hardware optimizations, as well as extensions to the measurement protocols, can be expected to allow significant gains in yield and SPAM performance in future. Our results indicate that asymmetric errors in erasure detection can introduce a bias in the measured outcomes, particularly for longer circuits where the erasure fraction is high, and so ways to estimate and mitigate these effects should be pursued.

The ability to perform high-fidelity preparation and measurement is a vital tool for all further characterization of dual-rail erasure qubits, including other critical operations such as mid-circuit erasure detection and two-qubit gates [53]. Combined, these will complete a full toolbox of error-detected quantum operations for the dual-rail cavity architecture. Confirmation of the expected error hierarchy, not only while idling, but also while performing these operations, could accelerate progress to fault-tolerant computing. Leakage detection in a single dual-rail qubit is an important first step on the path to correct erasures, which will require a next-level code made by concatenating many dual-rail qubits. The ability to detect or convert decoherence errors into measurable erasures opens new avenues for error mitigation and improving the effective fidelity of short-depth circuits.

**Acknowledgments** We thank the broader mechanical and control system groups at QCI, particularly Caleb Clothier, Richard Chamberlin, Michael Maxwell, and Charles Wehr. **Funding:** This research was supported by the U.S. Army Research Office (ARO) under grant W911NF-23-1-0051, and by the U.S. Department of Energy, Office of Science, National Quantum Information Science Research Centers, Co-design Center for Quantum Advantage (C2QA) under contract number DE-SC0012704. The views and conclusions contained in this document are those of the authors and should not be interpreted as representing official policies, either expressed or implied, of the ARO or the U.S. Government. The U.S. Government is authorized to reproduce and distribute reprints for Government purpose notwithstanding any copyright notation herein. **Competing interests:** Robert Schoelkopf and Luigi Frunzio are founders and shareholders of Quantum Circuits, Inc (QCI). Shruti Puri and Steven Girvin receive consulting fees and/or are equity holders in QCI. Authors affiliated with QCI have financial interest in the company.

[1] M. Mirrahimi, Z. Leghtas, V. V. Albert, S. Touzard, R. J. Schoelkopf, L. Jiang, and M. H. Devoret, Dynamically Protected Cat-Qubits: A New Paradigm for Universal Quantum Computation, New Journal of Physics **16**, 045014 (2014).

[2] M. H. Michael, M. Silveri, R. T. Brierley, V. V. Albert, J. Salmilehto, L. Jiang, and S. M. Girvin, New Class of Quantum Error-Correcting Codes for a Bosonic Mode, Phys. Rev. X **6**, 031006 (2016).

[3] A. Joshi, K. Noh, and Y. Y. Gao, Quantum Information Processing with Bosonic Qubits in Circuit QED, Quantum Science and Technology **6**, 033001 (2021).

[4] W. Cai, Y. Ma, W. Wang, C.-L. Zou, and L. Sun, Bosonic Quantum Error Correction Codes in Superconducting Quantum Circuits, Fundamental Research **1**, 50 (2021).

[5] W.-L. Ma, S. Puri, R. J. Schoelkopf, M. H. Devoret, S. M. Girvin, and L. Jiang, Quantum Control of Bosonic Modes with Superconducting Circuits, Science Bulletin **66**, 1789 (2021).

[6] N. Ofek, A. Petrenko, R. Heeres, P. Reinhold, Z. Leghtas, B. Vlastakis, Y. Liu, L. Frunzio, S. M. Girvin, L. Jiang, M. Mirrahimi, M. H. Devoret, and R. J. Schoelkopf, Extending the Lifetime of a Quantum Bit with Error Correction in Superconducting Circuits, Nature **536**, 441 (2016).

[7] V. V. Sivak, A. Eickbusch, B. Royer, S. Singh, I. Tsioutsios, S. Ganjam, A. Miano, B. L. Brock, A. Z. Ding, L. Frunzio, S. M. Girvin, R. J. Schoelkopf, and M. H. Devoret, Real-Time Quantum Error Correction Beyond Break-Even, Nature **616**, 50 (2023).

[8] Z. Ni, S. Li, X. Deng, Y. Cai, L. Zhang, W. Wang, Z.-B. Yang, H. Yu, F. Yan, S. Liu, C.-L. Zou, L. Sun, S.-B. Zheng, Y. Xu, and D. Yu, Beating the Break-Even Point with a Discrete-Variable-Encoded Logical Qubit, Nature **616**, 56 (2023).

[9] L. Hu, Y. Ma, W. Cai, X. Mu, Y. Xu, W. Wang, Y. Wu, H. Wang, Y. P. Song, C.-L. Zou, S. M. Girvin, L.-M. Duan, and L. Sun, Quantum Error Correction and Universal Gate Set Operation on a Binomial Bosonic Logical Qubit, Nature Physics **15**, 503 (2019).

[10] P. Aliferis and J. Preskill, Fault-Tolerant Quantum Computation Against Biased Noise, Phys. Rev. A **78**, 052331 (2008).

[11] D. K. Tuckett, A. S. Darmawan, C. T. Chubb, S. Bravyi, S. D. Bartlett, and S. T. Flammia, Tailoring Surface Codes for Highly Biased Noise, Physical Review X **9**, 041031 (2019).

[12] J. Guillaud and M. Mirrahimi, Repetition Cat Qubits for Fault-Tolerant Quantum Computation, Physical Review X **9**, 041053 (2019).

[13] A. S. Darmawan, B. J. Brown, A. L. Grimsmo, D. K. Tuckett, and S. Puri, Practical Quantum Error Correction with the XZZX Code and Kerr-Cat Qubits, PRX Quantum **2**, 030345 (2021).

[14] J. Claes, J. E. Bourassa, and S. Puri, Tailored Cluster States with High Threshold under Biased Noise, npj Quantum Information **9**, 1 (2023).

[15] P. Aliferis, F. Brito, D. P. DiVincenzo, J. Preskill, M. Steffen, and B. M. Terhal, Fault-Tolerant Computing with Biased-Noise Superconducting Qubits: a Case Study, New Journal of Physics **11**, 013061 (2009).

[16] A. Grimm, N. E. Frattini, S. Puri, S. O. Mundhada, S. Touzard, M. Mirrahimi, S. M. Girvin, S. Shankar, and M. H. Devoret, Stabilization and Operation of a Kerr-Cat Qubit, Nature **584**, 205 (2020).

[17] S. Puri, L. St-Jean, J. A. Gross, A. Grimm, N. E. Frattini, P. S. Iyer, A. Krishna, S. Touzard, L. Jiang, A. Blais, S. T. Flammia, and S. M. Girvin, Bias-Preserving Gates with Stabilized Cat Qubits, Science Advances **6**, eaay5901 (2020).

[18] R. Lescanne, M. Villiers, T. Peronnin, A. Sarlette, M. Delbecq, B. Huard, T. Kontos, M. Mirrahimi, and Z. Leghtas, Exponential Suppression of Bit-Flips in a Qubit Encoded in an Oscillator, Nature Physics **16** (2020).

[19] C. Berdou, A. Murani, U. Reglade, W. C. Smith, M. Villiers, J. Palomo, M. Rosticher, A. Denis, P. Morfin, M. Delbecq, T. Kontos, N. Pankratova, F. Rautschke, T. Peronnin, L.-A. Sellem, P. Rouchon, A. Sarlette, M. Mirrahimi, P. Campagne-Ibarcq, S. Jezouin, R. Lescanne, and Z. Leghtas, One Hundred Second Bit-Flip Time in a Two-Photon Dissipative Oscillator (2022), arXiv:2204.09128.

[20] R. Chao and B. W. Reichardt, Flag Fault-Tolerant Error Correction for any Stabilizer Code, PRX Quantum **1**, 010302 (2020).

[21] C. Chamberland, G. Zhu, T. J. Yoder, J. B. Hertzberg, and A. W. Cross, Topological and Subsystem Codes on Low-Degree Graphs with Flag Qubits, Physical Review X **10**, 011022 (2020).

[22] C. Ryan-Anderson, J. Bohnet, K. Lee, D. Gresh, A. Hankin, J. Gaebler, D. Francois, A. Chernoguzov, D. Lucchetti, N. Brown, T. Gatterman, S. Halit, K. Gilmore, J. Gerber, B. Neyenhuis, D. Hayes, and R. Stutz, Realization of Real-Time Fault-Tolerant Quantum Error Correction, Physical Review X **11**, 041058 (2021).

[23] C. Ryan-Anderson, N. C. Brown, M. S. Allman, B. Arkin, G. Asa-Attuah, C. Baldwin, J. Berg, J. G. Bohnet, S. Braxton, N. Burdick, J. P. Campora, A. Chernoguzov, J. Esposito, B. Evans, D. Francois, J. P. Gaebler, T. M. Gatterman, J. Gerber, K. Gilmore, D. Gresh, A. Hall, A. Hankin, J. Hostetter, D. Lucchetti, K. Mayer, J. Myers, B. Neyenhuis, J. Santiago, J. Sedlacek, T. Skripka, A. Slattery, R. P. Stutz, J. Tait, R. Tobey, G. Vittorini, J. Walker, and D. Hayes, Implementing Fault-tolerant Entangling Gates on the Five-qubit Code and the Color Code (2022), arXiv:2208.01863.

[24] E. H. Chen, T. J. Yoder, Y. Kim, N. Sundaresan, S. Srinivasan, M. Li, A. D. Córcoles, A. W. Cross, and M. Takita, Calibrated Decoders for Experimental Quantum Error Correction (2022), arXiv:2110.04285.

[25] M. Grassl, T. Beth, and T. Pellizzari, Codes for the Quantum Erasure Channel, Phys. Rev. A **56**, 33 (1997).

[26] Y. Wu, S. Kolkowitz, S. Puri, and J. D. Thompson, Erasure Conversion for Fault-Tolerant Quantum Computing in Alkaline Earth Rydberg Atom Arrays, Nature Communications **13**, 4657 (2022).

[27] A. Kubica, A. Haim, Y. Vaknin, F. Brandão, and A. Retzker, Erasure Qubits: Overcoming the $T_1$ Limit in Superconducting Circuits (2022), arXiv:2208.05461.

[28] P. Scholl, A. L. Shaw, R. B.-S. Tsai, R. Finkelstein, J. Choi, and M. Endres, Erasure conversion

in a high-fidelity rydberg quantum simulator (2023), arXiv:2305.03406.
[29] S. Ma, G. Liu, P. Peng, B. Zhang, S. Jandura, J. Claes, A. P. Burgers, G. Pupillo, S. Puri, and J. D. Thompson, High-fidelity gates with mid-circuit erasure conversion in a metastable neutral atom qubit (2023), arXiv:2305.05493.
[30] T. M. Stace, S. D. Barrett, and A. C. Doherty, Thresholds for Topological Codes in the Presence of Loss (2009).
[31] S. D. Barrett and T. M. Stace, Fault Tolerant Quantum Computation with Very High Threshold for Loss Errors, Phys. Rev. Lett. **105**, 200502 (2010).
[32] I. L. Chuang and Y. Yamamoto, Simple Quantum Computer, Physical Review A **52**, 3489 (1995).
[33] E. Knill, R. Laflamme, and G. J. Milburn, A Scheme for Efficient Quantum Computation with Linear Optics, Nature **409**, 46 (2001).
[34] P. Kok, W. J. Munro, K. Nemoto, T. C. Ralph, J. P. Dowling, and G. J. Milburn, Linear Optical Quantum Computing with Photonic Qubits, Reviews of Modern Physics **79**, 135 (2007).
[35] S. Bartolucci, P. Birchall, H. Bombín, H. Cable, C. Dawson, M. Gimeno-Segovia, E. Johnston, K. Kieling, N. Nickerson, M. Pant, F. Pastawski, T. Rudolph, and C. Sparrow, Fusion-Based Quantum Computation, Nature Communications **14**, 912 (2023).
[36] J. D. Teoh, P. Winkel, H. K. Babla, B. J. Chapman, J. Claes, S. J. de Graaf, J. W. O. Garmon, W. D. Kalfus, Y. Lu, A. Maiti, K. Sahay, N. Thakur, T. Tsunoda, S. H. Xue, L. Frunzio, S. M. Girvin, S. Puri, and R. J. Schoelkopf, Dual-rail encoding with superconducting cavities (2022), arXiv:2212.12077.
[37] S. Rosenblum, P. Reinhold, M. Mirrahimi, L. Jiang, L. Frunzio, and R. J. Schoelkopf, Fault-Tolerant Detection of a Quantum Error, Science **361**, 266 (2018).
[38] P. Reinhold, S. Rosenblum, W.-L. Ma, L. Frunzio, L. Jiang, and R. J. Schoelkopf, Error-Corrected Gates on an Encoded Qubit, Nature Physics **16**, 822 (2020).
[39] Y. Ma, Y. Xu, X. Mu, W. Cai, L. Hu, W. Wang, X. Pan, H. Wang, Y. P. Song, C.-L. Zou, and L. Sun, Error-Transparent Operations on a Logical Qubit Protected by Quantum Error Correction, Nature Physics **16**, 827 (2020).
[40] B. J. Chapman, S. J. de Graaf, S. H. Xue, Y. Zhang, J. Teoh, J. C. Curtis, T. Tsunoda, A. Eickbusch, A. P. Read, A. Koottandavida, S. O. Mundhada, L. Frunzio, M. Devoret, S. Girvin, and R. Schoelkopf, High-on-off-ratio beam-splitter interaction for gates on bosonically encoded qubits, PRX Quantum **4**, 020355 (2023).
[41] Y. Lu, A. Maiti, J. W. O. Garmon, S. Ganjam, Y. Zhang, J. Claes, L. Frunzio, S. M. Girvin, and R. J. Schoelkopf, A High-Fidelity Microwave Beamsplitter with a Parity-Protected Converter (2023), arXiv:2303.00959.
[42] S. J. de Graaf *et al.*, In preparation.
[43] N. E. Frattini, U. Vool, S. Shankar, A. Narla, K. M. Sliwa, and M. H. Devoret, 3-Wave Mixing Josephson Dipole Element, Applied Physics Letters **110**, 222603 (2017).
[44] L. Verney, R. Lescanne, M. H. Devoret, Z. Leghtas, and M. Mirrahimi, Structural Instability of Driven Josephson Circuits Prevented by an Inductive Shunt, Phys. Rev. Appl. **11**, 024003 (2019).
[45] J. Gambetta, W. A. Braff, A. Wallraff, S. M. Girvin, and R. J. Schoelkopf, Protocols for Optimal Readout of Qubits Using a Continuous Quantum Nondemolition Measurement, Phys. Rev. A **76**, 012325 (2007).
[46] S. S. Elder, C. S. Wang, P. Reinhold, C. T. Hann, K. S. Chou, B. J. Lester, S. Rosenblum, L. Frunzio, L. Jiang, and R. J. Schoelkopf, High-Fidelity Measurement of Qubits Encoded in Multilevel Superconducting Circuits, Phys. Rev. X **10**, 011001 (2020).
[47] R. W. Heeres, P. Reinhold, N. Ofek, L. Frunzio, L. Jiang, M. H. Devoret, and R. J. Schoelkopf, Implementing a universal gate set on a logical qubit encoded in an oscillator, Nature Communications **8**, 94 (2017).
[48] J. C. Curtis, C. T. Hann, S. S. Elder, C. S. Wang, L. Frunzio, L. Jiang, and R. J. Schoelkopf, Single-Shot Number-Resolved Detection of Microwave Photons with Error Mitigation, Physical Review A **103**, 023705 (2021).
[49] A. G. Fowler, Coping with Qubit Leakage in Topological Codes, Phys. Rev. A **88**, 042308 (2013).
[50] J. Ghosh, A. G. Fowler, J. M. Martinis, and M. R. Geller, Understanding the Effects of Leakage in Superconducting Quantum-Error-Detection Circuits, Phys. Rev. A **88**, 062329 (2013).
[51] C. C. Bultink, T. E. O'Brien, R. Vollmer, N. Muthusubramanian, M. W. Beekman, M. A. Rol, X. Fu, B. Tarasinski, V. Ostroukh, B. Varbanov, A. Bruno, and L. DiCarlo, Protecting quantum entanglement from leakage and qubit errors via repetitive parity measurements, Science Advances **6**, eaay3050 (2020).
[52] M. McEwen, D. Kafri, Z. Chen, J. Atalaya, K. J. Satzinger, C. Quintana, P. V. Klimov, D. Sank, C. Gidney, A. G. Fowler, F. Arute, K. Arya, B. Buckley, B. Burkett, N. Bushnell, B. Chiaro, R. Collins, S. Demura, A. Dunsworth, C. Erickson, B. Foxen, M. Giustina, T. Huang, S. Hong, E. Jeffrey, S. Kim, K. Kechedzhi, F. Kostritsa, P. Laptev, A. Megrant, X. Mi, J. Mutus, O. Naaman, M. Neeley, C. Neill, M. Niu, A. Paler, N. Redd, P. Roushan, T. C. White, J. Yao, P. Yeh, A. Zalcman, Y. Chen, V. N. Smelyanskiy, J. M. Martinis, H. Neven, J. Kelly, A. N. Korotkov, A. G. Petukhov, and R. Barends, Removing Leakage-Induced Correlated Errors in Superconducting Quantum Error Correction, Nature Communications **12**, 1761 (2021).
[53] T. Tsunoda, J. D. Teoh, W. D. Kalfus, S. J. de Graaf, B. J. Chapman, J. C. Curtis, N. Thakur, S. M. Girvin, and R. J. Schoelkopf, Error-Detectable Bosonic Entangling Gates with a Noisy Ancilla, PRX Quantum **4**, 020354 (2023).
[54] T. Thorbeck, Z. Xiao, A. Kamal, and L. C. G. Govia, Readout-Induced Suppression and Enhancement of Superconducting Qubit Lifetimes (2023), arXiv:2305.10508.
[55] E. Magesan, J. M. Gambetta, and J. Emerson, Scalable and Robust Randomized Benchmarking of Quantum Processes, Phys. Rev. Lett. **106**, 180504 (2011).
[56] Qiskit contributors, Qiskit: An Open-Source Framework for Quantum Computing (2023).
[57] A. Blais, A. L. Grimsmo, S. M. Girvin, and A. Wallraff, Circuit quantum electrodynamics, Rev. Mod. Phys. **93**, 025005 (2021).
[58] A. Blais, R.-S. Huang, A. Wallraff, S. M. Girvin, and R. J. Schoelkopf, Cavity quantum electrodynamics for superconducting electrical circuits: An architecture for quantum computation, Phys. Rev. A **69**, 062320 (2004).
[59] J. Johansson, P. Nation, and F. Nori, Qutip: An Open-Source Python Framework for the Dynamics of Open Quantum Systems, Computer Physics Communications

**183**, 1760 (2012).
[60] J. Johansson, P. Nation, and F. Nori, Qutip 2: A Python Framework for the Dynamics of Open Quantum Systems, Computer Physics Communications **184**, 1234 (2013).
[61] V. Siddhu, A. Chatterjee, K. Jagannathan, P. Mandayam, and S. Tayur, Queue-Channel Capacities with Generalized Amplitude Damping (2021), arXiv:2107.13486.
[62] M. A. Nielsen and I. L. Chuang, *Quantum Computation and Quantum Information: 10th Anniversary Edition* (Cambridge University Press, 2010).
[63] L. B.-V. Horn, sequencing-dev/sequencing: v1.2.0 10.5281/zenodo.7036085 (2022).

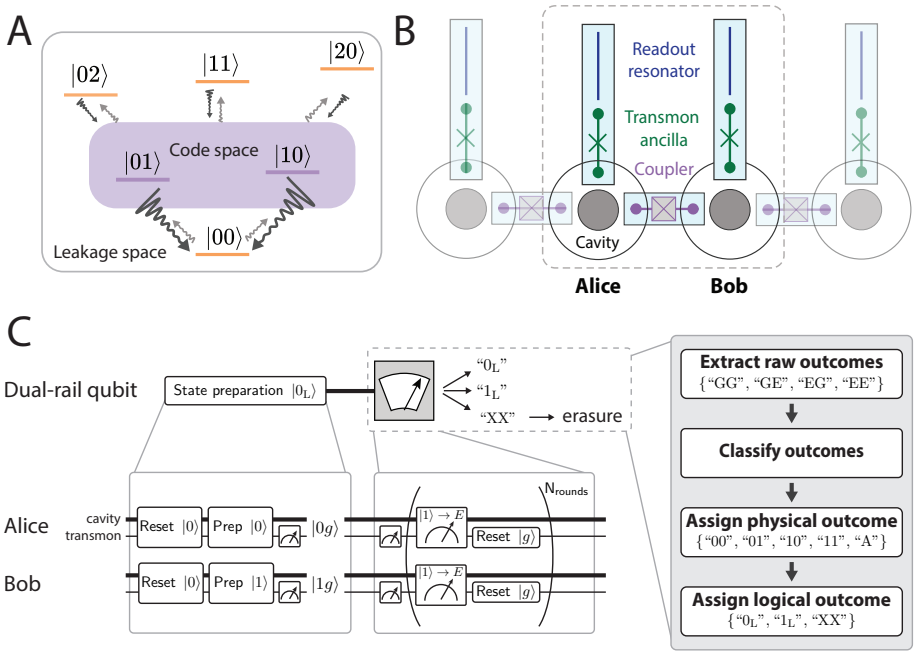


FIG. 1. **Dual-rail qubit concept, implementation, and measurement.** (A) The dual-rail codespace spans the states $\{|01\rangle, |10\rangle\}$. Transitions out of the codespace induced by either relaxation or heating events bring the system into a leakage space that can be detected with the appropriate measurement protocol. (B) The dual-rail qubit is implemented in a superconducting cQED module consisting of several physical modes: two superconducting cavities here implemented as three-dimensional $\lambda/4$-coaxial cavities (gray), and each dispersively coupled to a transmon (green) and a resonator (blue) for control and readout. Single-qubit operations are engineered by beamsplitter interactions [40, 41] enabled by a nonlinear coupler, here constructed as an array of three SNAIL elements operated at the zero-bias sweet-spot [43, 44], resulting in single-qubit gate fidelities as shown in Supplementary Materials. There are adjacent cavity systems within this module that are not used in this experiment, shown as shaded elements. (C) Logical state preparation and measurement protocols used in this work. The dual-rail logical measurement incorporates erasure detection, leading to a measurement with three outcomes: logical outcomes "$0_L$" and "$1_L$", and erasures. There are several steps required to decode the logical measurement, starting with assignment of the transmon outcomes, classification and assignment to one of the physical cavity outcomes ("00", "01", "10", or "11") or to an ambiguous outcome ("A") in the case of multiple rounds of measurements disagreeing, before finally assigning the logical outcome.

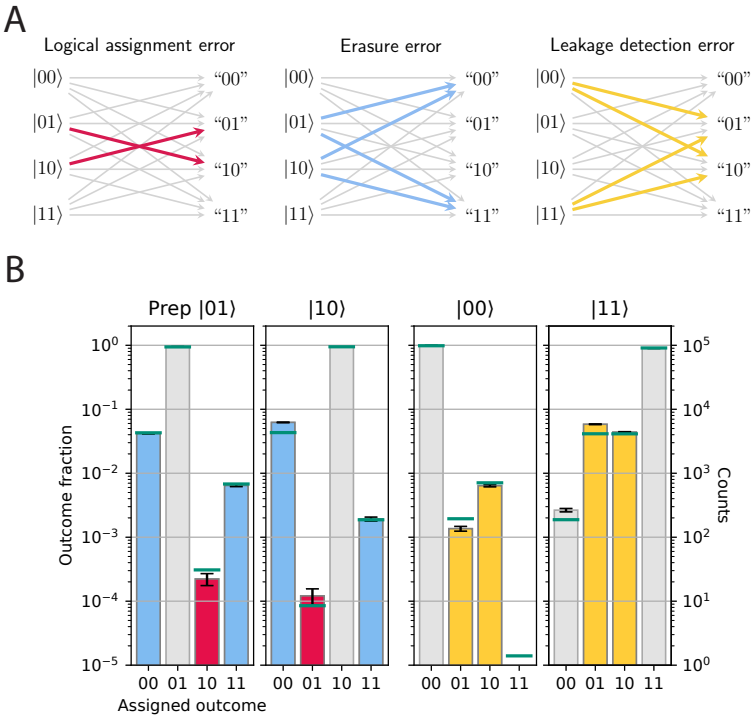


FIG. 2. **State preparation and measurement of a dual-rail qubit.** (A) The set of possible measurement outcomes can be summarized in the assignment channel diagram, color-coded to highlight several different figures of merit. Apparent bit-flip errors (pink) are a logical misassignment of $|01\rangle$ for $|10\rangle$ and vice versa. Erasure errors (blue) indicate an erasure outcome was measured despite preparation in one of the logical states. Finally, leakage detection errors (yellow) are misassignments of a known leaked state: e.g. $|00\rangle$ or, less likely $|11\rangle$. (B) State assignment data using 1 round of measurements. In our SPAM experiment, we prepare each of the four dual-rail states and perform a logical measurement. Results for each dual-rail state are shown in each panel; and each bar corresponds to a different assigned physical state. The model results are shown as blue lines for each outcome. Error bars represent the standard error, showing $\pm 1\sigma$.

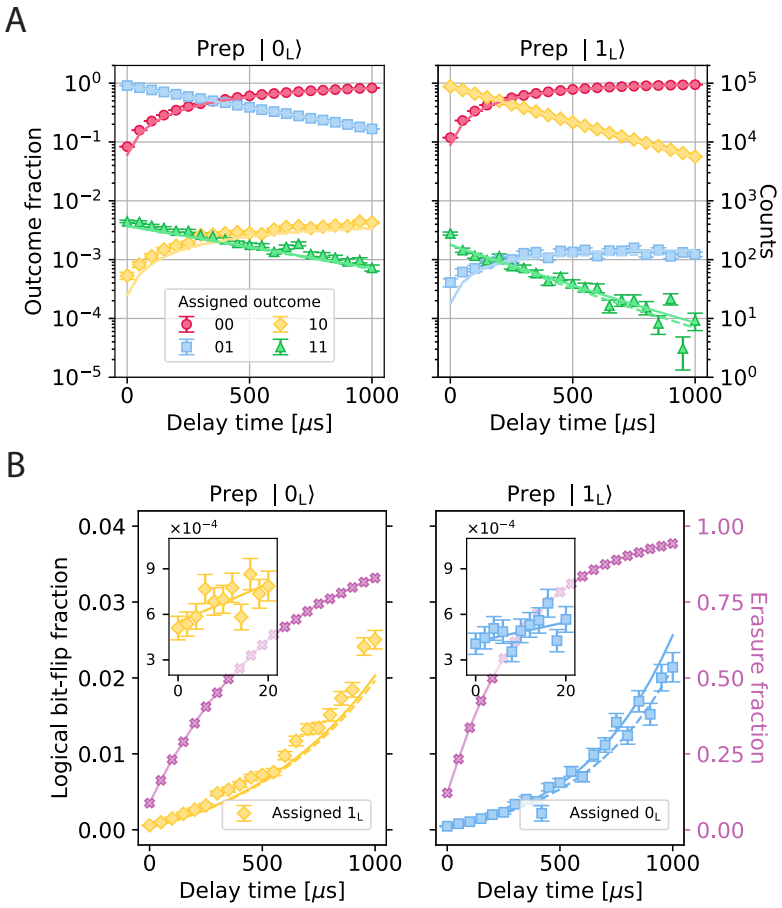


FIG. 3. **Dual-rail bit-flip error measurement.** (A) Assigned physical state outcomes measured as a function of delay for the dual-rail cavity qubit prepared in $|0_L\rangle$ (left) and $|1_L\rangle$ (right). The occurrence of each measured outcome is shown both as a fraction (left axis) and as total counts (right axis). The solid line corresponds to a simulation performed with measured parameters; the dashed line is a simulation performed without any intrinsic bit-flip errors by setting the cavity heating rates to zero. (B) We compute the logical outcomes and plot the bit-flip error fraction when initializing in $|0_L\rangle$ (left) and $|1_L\rangle$ (right). The solid and dashed lines are generated using the same simulations as in Fig. 3a, both showing good agreement with the data. The small difference between the two simulations provide evidence that intrinsic bit-flip errors are yet a small contribution to the apparent bit-flip error. The inset shows results for an additional experiment performed with delays out to 20 $\mu$s. We perform a linear fit (solid line) and extract an apparent bit-flip error rate of $(0.00063 \pm 0.00038)\,\%$ and $(0.0013 \pm 0.00039)\,\%$ in a microsecond, for $|0_L\rangle$ (left) and $|1_L\rangle$, respectively.

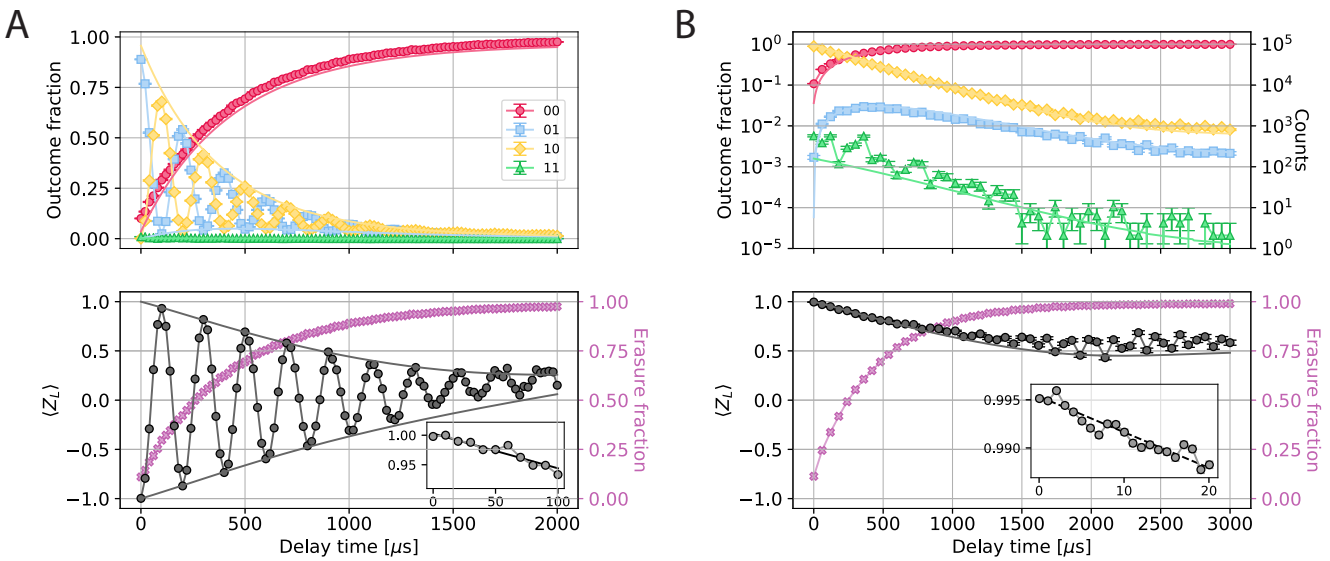


FIG. 4. **Dual-rail phase error measurement.** (A) Dual-rail qubit Ramsey and (B) echo experiment showing the assigned physical outcomes in the top panel; the logical outcome $\langle Z_{\mathrm{L}} \rangle$ (black circles) and erasure fraction (purple x-markers) are shown in the bottom panel. Simulation results are shown in solid lines. The inset shows results from an additional experiment performed with shorter delays and the black line is a linear fit to the data. We extract dephasing error rates of $(0.059 \pm 0.006)\%$ and $(0.037 \pm 0.003)\%$ in a microsecond for the Ramsey and echo experiments, respectively.

## SUPPLEMENTARY MATERIALS

## MATERIALS AND METHODS

### System Properties

| | Description | Parameter | Units | **Alice** | **Bob** |
|---|---|---|---|---|---|
| **System** | Cavity-transmon cross-kerr | $\chi_{\mathrm{cm}}/2\pi$ | MHz | -2.14 | -3.72 |
| | Cavity-coupler cross-kerr | $\chi_{\mathrm{cc}}/2\pi$ | kHz | -99 | -110 |
| **Cavity** | Relaxation time | $T_1^{\mathrm{c}}$ | $\mu$s | 592 | 350 |
| | Dephasing time, Ramsey | $T_{2\mathrm{R}}^{\mathrm{c}}$ | $\mu$s | 768 | 543 |
| | Dephasing time, Echo | $T_{2\mathrm{E}}^{\mathrm{c}}$ | $\mu$s | 932 | 588 |
| | Thermal population | $n_{\mathrm{th}}^{\mathrm{c}}$ | % | 0.035 * | 0.017 * |
| | Self-kerr | $K/2\pi$ | kHz | -5.79 | -11.02 |
| | Resonance frequency | $\omega_{\mathrm{c}}/2\pi$ | GHz | 7.16 | 6.76 |
| **Transmon** | Relaxation time | $T_1^{\mathrm{t}}$ | $\mu$s | 125 | 179 |
| | Dephasing time, Ramsey | $T_{2\mathrm{R}}^{\mathrm{t}}$ | $\mu$s | 92 | 206 |
| | Dephasing time, Echo | $T_{2\mathrm{E}}^{\mathrm{t}}$ | $\mu$s | 144 | 303 |
| | Thermal population | $n_{\mathrm{th}}^{\mathrm{t}}$ | % | 1 | 1 |
| | Anharmonicity | $\alpha/2\pi$ | MHz | -184.63 | -185.71 |
| | Resonance frequency | $\omega_{\mathrm{t}}/2\pi$ | GHz | 4.83 | 4.92 |
| | Selective $\pi$-pulse sigma | $\sigma_{\mathrm{s}}$ | ns | 300 | 300 |
| | Unselective $\pi$-pulse sigma | $\sigma_{\mathrm{us}}$ | ns | 16 | 16 |
| **Readout** | Duration | $t_{\mathrm{M}}$ | $\mu$s | 2.0 | 3.6 |
| | Processing time | $t_d$ | $\mu$s | 0.4 | 0.4 |
| | Transmon relaxation time during readout | $T_{1\ \mathrm{RO}}^{\mathrm{t}}$ | $\mu$s | 80 * | 100 * |
| | Transmon Thermal population during readout | $n_{\mathrm{th\ RO}}^{\mathrm{t}}$ | % | 2 * | 11 * |
| | Prob. of misassigning $\|g\rangle$ as $\|e\rangle$ | $p_{\mathrm{gE}}$ | $\times 10^{-3}$ | 1.00 * | 3.22 * |
| | Prob. of misassigning $\|e\rangle$ as $\|g\rangle$ | $p_{\mathrm{eG}}$ | $\times 10^{-3}$ | 4.03 * | 1.18 * |

* See subsequent sections for details of these measurements.

#### *Measurement of Cavity Thermal Population*

We bound the cavity thermal population $n_{\mathrm{th}}^{c}$ by conducting a modified bit-flip experiment. This is particularly important as cavity heating is expected to be the main mechanism for actual transitions. The measurement is performed as follows: the dual-rail qubit is prepared in the physical state $|00\rangle$, and after a variable time-delay the resulting state is measured in order to measure any transitions to excited states due to cavity heating.

The results of the measurement are shown in Fig. 5. Given that we expect errors associated with the measurement (misassignment errors) to dominate over those due to cavity heating, we measure twice after the time-delay. Each of the two measurements of the cavity states must agree, or the result is labeled "A" (ambiguous) and thrown out; this suppresses the misassignment error. With the two measurements, the excited states ($|01\rangle$ and $|10\rangle$) show a behavior typical of heating, where the probability of the states increases and then saturates at long time. We bound the cavity $n_{\mathrm{th}}^{c}$ to be less than $4 \times 10^{-4}$ by examining the long time, saturated behavior. This value for the average cavity occupation suppresses the rate of actual transitions between logical states, which would then be estimated to be $< 500$ ppm in one microsecond, or a remarkably low rate of $1/(\sim 2000$ seconds) in the absence of other intrinsic bit-flip processes, and assuming ideal state preparation.

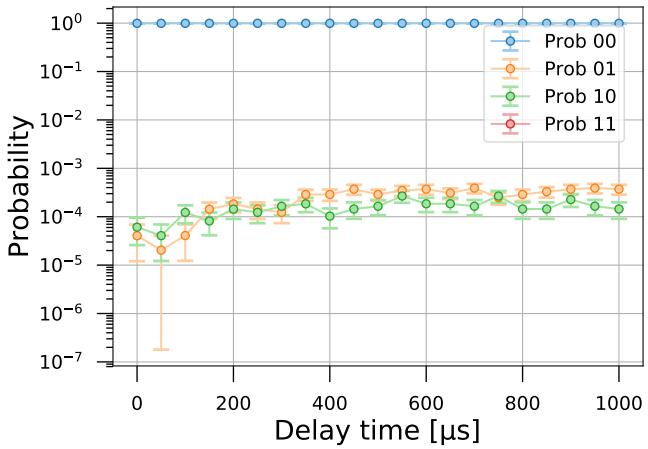


FIG. 5. (a) **Measurement of cavity** $n_{th}$ Plot of physical state probability as a function of delay time after being prepared in the ground state $|00\rangle$. We perform this experiment to measure the cavity heating, which sets the limit of the intrinsic bit-flip rate. Given that misassignment dominates over the cavity heating, we use two end-of-line measurements to suppress the measurement error. We interpret the long-time behavior where the excited states ($|01\rangle$ and $|10\rangle$) saturate as bounding the cavity heating rate.

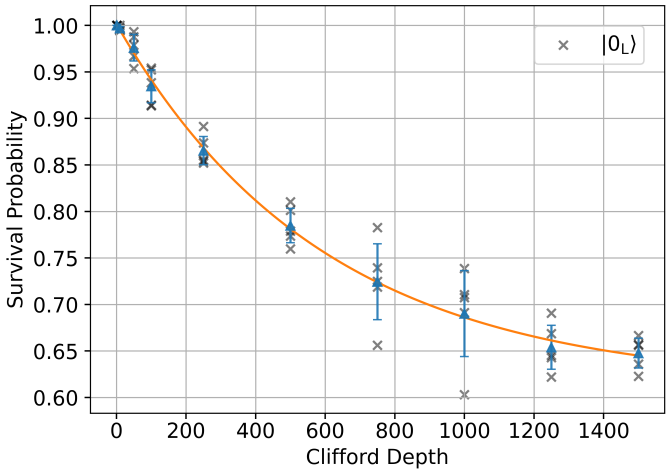


FIG. 6. **Single-qubit randomized benchmarking (RB) measurement** We perform single-qubit randomized benchmarking in the dual-rail basis with five seeds (represented by x) at each Clifford Depth. The single-qubit gates are used in this paper when measuring the phase error rates. The mean (triangle) measured survival probability is fit to a exponential and from this we extract the error-per-Clifford as $8.4 \times 10^{-4}$.

*Measurement of Readout Properties*

We measure the readout properties of our transmons with two experiments.

First, we measure $T_1$ during readout by performing a "$T_1$ vs. $\bar{n}$" experiment on each of the ancilla transmons. We perform this experiment with the insight that due to the well-known effect where the transmon lifetime gets suppressed at certain readout amplitudes, there may be an increased probability of a transition event during readout [54]. As the measured system properties are the input for both of our models (see Supplementary Text), our aim is to characterize all aspects of our system accurately, including any changes to coherences during readout.

In the experiment, we choose an array of values for the pulse amplitude; for each pulse amplitude we perform a $T_1$ experiment on the transmon (excite the transmon to $|e\rangle$ and measure the probability of it remaining in $|e\rangle$ for variable delays between preparation and measurement) while driving the readout tone at the chosen amplitude. We fit the data at each point to a decaying exponential and extract $T_{1\,RO}^{(t)}$ at the readout amplitudes we use.

We also know that the transmons may suffer some residual heating during readout compared to their ambient

thermal populations. In order to extract a value for the effective transmon thermal population during readout, $n^{(t)}_{th\ RO}$, we examine the offsets of the fits to the data as described above.

Second, in order to extract $p_{gE}$ and $p_{eG}$, we perform an experiment where we prepare the transmon in $|g\rangle$ and then repeatedly measure it 10 times; we repeat the experiment $10^5$ times. In this experiment the signature of a transition is different from the signature of a misassignment, as in the former case consecutive measurements will have the same outcome and in the latter case they will not. We average over the traces of all runs of the experiment, and from the signature traces of misassignments we extract the probabilities of misassigning $|g\rangle$ as $E$, and $|e\rangle$ as $G$.

### Single-Qubit Gate Benchmarking

In this paper, the single-qubit gates are used when measuring the phase error rates. We characterize the quality of the gates using single-qubit randomized benchmarking [55, 56] in the dual-rail space. As shown in Fig. 6, the resulting error-per-Clifford (EPC) from this measurement is $8.4 \times 10^{-4}$. This rate is obtained by generating five seeds across Clifford depths ranging from 0 to 1500. The physical gates are comprised of 50-50 beamsplitters ($\pi/2$) and SWAPs ($\pi$). We plot the survival probability, meaning the prepared state is returned, as a function of Clifford depth.

### cQED Toolbox for Bosonic Operations

All operations necessary for state preparation, measurement, and reset of the dual-rail cavity qubit are implemented using the now well-established cQED toolbox of operations [57]. This includes all the operations necessary for state preparation, measurement, and system reset of the dual-rail qubit.

In the subsequent sections we explain each element of the dual-rail qubit's toolbox in some detail.

#### *Mapping*

Measurement of the cavity state is realized by mapping the state to the cavity's ancilla transmon, before performing a subsequent readout of the transmon in order to infer the state of the cavity.

In the data presented in this paper, the mapping was implemented by way of a selective $\pi$-pulse on the ancilla transmon; the pulse was executed as a truncated Gaussian pulse. Specifically, this means that we perform a $\pi$-pulse on the transmon–conditioned on the cavity being in the Fock state $|n\rangle$:

$$X^s_n = |n\rangle\langle n| \otimes \hat{\sigma}_x + \sum_{m \neq n} |m\rangle\langle m| \otimes \hat{I}$$

The ancilla is dispersively coupled to the cavity with its resonance frequency given by $\tilde{\omega}_q = \omega_q - n\chi$, where $\omega_q$ is the transmon's bare resonance frequency, $n$ is the number of photons in the cavity, and $\chi$ is the cavity-transmon cross-Kerr. This interaction dictates our two main degrees of freedom in tailoring the selective-pulse mapping for our dual-rail protocol.

First, we choose the pulse duration. The pulse, in the time domain, is parameterized as $chop \cdot \sigma$, where $\sigma$ is the standard deviation of the Gaussian pulse that is truncated at $\pm chop/2$ standard deviations of the Gaussian. In the frequency domain, the bandwidth of the pulse is given by $1/(2\pi\sigma)$, and as such given the cross-Kerrs of our subsystems, we choose a pulse sigma that is long enough such that the pulse's bandwidth is narrow enough to be sufficiently selective on one of the Fock states $|n\rangle$. We choose our pulse sigmas by numerically computing the unselectivity error of the pulse as $Err = 1 - |\langle 1, g|X^s_{n=0}|1, g\rangle|^2$ taking $\chi$ and $\sigma$ into account.

Second, we can choose the frequency of of the selective-pulse for the mapping. Namely, we can detune the pulse by $n\chi$, where $n$ is any integer and will lead to the transmon being rotated conditioned on the cavity being in the Fock state $|n\rangle$. In our dual-rail protocol, the dominant leakage mechanism is cavity decay events to the $|00\rangle$ state. As such, in order to minimize the misassignment of leakage states to the codespace, we detune our selective pulses by $\chi$ such that we obtain the following cavity-to-transmon mapping:

$$|0\rangle \rightarrow |g\rangle$$
$$|1\rangle \rightarrow |e\rangle$$

and the dual-rail leakage state $|00\rangle$ maps to $|gg\rangle$ rather than to the more error-prone state (for readout purposes) $|ee\rangle$.

*Transmon Readout*

Transmon readout in the dual-rail protocol is realized by way of standard dispersive readout [58].

In tailoring the transmon readout to the dual-rail protocol, one primary degree of freedom that we have is the readout pulse's duration.

In choosing the readout duration we seek to optimize the trade-off between readout separation and transitions during readout–that are inversely parameterized by the readout duration $t_M$. Specifically, the readout separation, or the distinguishability of the states in the IQ plane is characterized by the parameter $\bar{I}_m/\sigma$ that scales as $\sqrt{t_M}$; as such, the separation increases, and the classification error accordingly decreases as $t_M$ increases. However, transmon decay and heating events scale as $t_M/T_{1\ RO}^{(t)}$ and $n_{th\ RO}^{(t)} \cdot t_M/T_{1\ RO}^{(t)}$, respectively, and as such the probability of a transmon transition during readout (i.e. a non-QND measurement) increases as $t_M$ increases. We quantify these probabilities given our system parameters and choose $t_M$ accordingly in order to balance this trade-off.

*Conditional Reset*

In our dual-rail protocols, we always immediately reset the transmon back to the ground state $|g\rangle$ subsequent to it being rotated to $|e\rangle$ by any component of the protocol.

We perform this reset conditioned on having learned that the transmon is in $|e\rangle$, i.e. following a transmon readout, and implement it via an unselective $\pi$-pulse. An unselective pulse, in contrast with the selective pulse described in the Mapping section, is a short pulse in the time-domain or, equivalently a broad pulse in the frequency-domain that is thus intended to be unselective on the cavity photon-number.

We tailor this unselective $\pi$-pulse for the purpose of conditional reset with the same considerations in mind as when tailoring the selective pulse as described in the Mapping section.

First, we choose the pulse duration to be short enough such that it is sufficiently unselective given the system's $\chi$, with the error computed numerically as $\epsilon = 1 - |\langle 1, e|X_{n=0}^{us}|1, g\rangle|^2$, where $us$ denotes the unselective $\pi$-pulse. Specifically we want $1/(2\pi\sigma)$ to be large enough such that the pulse is broad enough in the frequency domain to rotate the transmon from $|e\rangle$ back to $|g\rangle$ regardless of whether the cavity is in the state $|0\rangle$ or $|1\rangle$.

Second, similar to the case of the selective pulse, we have a choice in the detuning of the unselective pulse. For the dual-rail protocol, we detune the unselective reset pulse by $\chi$, so that it is on resonance when the cavity is in the state $|1\rangle$. We do this, since given our mapping choice (as described in the Mapping section) the transmon is rotated to $|e\rangle$ when the cavity is in the state $|1\rangle$. Consequently, in our logical measurement protocol, when the transmon is measured to be in $|e\rangle$ after a mapping of the cavity state, the cavity is mostly likely in $|1\rangle$ and therefore the conditional reset is most likely to succeed if it is resonant when the cavity is in $|1\rangle$.

*Transmon Check*

The post-reset check is realized by way of a transmon readout, exactly as described in the Transmon Readout section, with the only difference being in the logic of the way the measurement outcome is processed.

In the dual-rail protocol, we perform these transmon checks at points in the protocol where a measurement outcome of $|e\rangle$ will indicate that an error has occurred. As such, in the cases where the measurement outcome of a check measurement is $|e\rangle$, that shot, or run of the experiment is discarded in post-selection, with this run of the experiment contributing statistically to runs where an erasure was detected.

*Cavity-State Initialization*

In the data presented in this paper, cavities were initialized in $|1\rangle$ using an optimal control pulse (OCP) [47], with a duration of 1 $\mu s$.

There are other methods of cavity-state initialization, such as sideband operations [37] to load a photon from the transmon to the cavity, or measurement-based approaches [46]. Exploring other such methods and optimizing state preparation for the purpose of the dual-rail qubit will be explored in future work.

### State Preparation and Measurement Protocols

Two primary overarching components of the dual-rail qubit operations are state preparation and measurement. Here we refer to the dual-rail measurement as a logical measurement, implying that it is a projective measurement of the logical $\hat{\sigma}_z$ operator.

We construct each of these protocols using the elements in our toolbox as described in the cQED Toolbox for Bosonic Operations section. In the subsequent section we describe the exact way in which we construct each protocol.

#### *State Preparation*

In order the prepare all of the dual-rail basis states in the 0 and 1-photon subspaces, we need to be able to prepare each cavity in the state $|0\rangle$ and in the state $|1\rangle$.

**Preparing the cavity in $|0\rangle$** Being able to prepare our cavities in $|0\rangle$ with high fidelity is of twofold importance. First, in our dual-rail experiments we perform many runs of each experiment in order to accumulate statistics and sufficiently resolve the outcomes that we want to measure. As such, we need an efficient way to reset the system, i.e. both the dual-rail's cavities and transmons to the ground state between each run. Second, as our logical basis is spanned by $\{|01\rangle, |10\rangle\}$, in order to prepare any logical state we must be able in turn to prepare each of the cavities in $|0\rangle$.

Specifically, our protocol for preparing a cavity in $|0\rangle$ is as follows. First, we perform a cavity measurement that consists of mapping the cavity-state to the transmon using a selective pulse followed by a readout of the ancilla transmon. As described in the Mapping section, this pulse is detuned by $\chi$ in order to map the correct outcome to $|g\rangle$ and mitigate assignment errors If the measurement outcome is $G$, indicating that the cavity is in $|0\rangle$, the cavity measurement is repeated $N$ times, until we get a string of six consecutive $G$ outcomes confirming that the cavity is indeed in $|0\rangle$. If the measurement outcome is $E$, indicating that the cavity is still in $|1\rangle$, we add a short delay of 10 $\mu s$ before restarting the whole process over again.

Second, we append a transmon check measurement (as described in the Transmon Check section) in order to confirm that the ancilla transmon is in the ground state before subsequent operations following the state preparation.

Represented as a circuit diagram, our prep $|0\rangle$ protocol is:

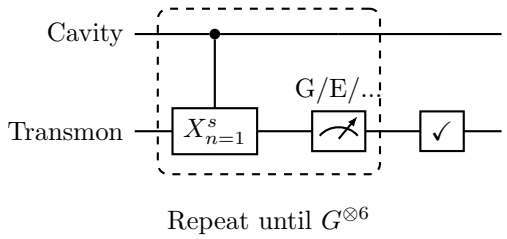


There are a number of alternatives to this protocol. These include sideband operations to SWAP an excitation from the cavity to the ancilla followed by a subsequent $\pi$-pulse on the ancilla to reset it to $|g\rangle$, different numbers of cavity measurements, or removing the appended transmon check. Investigating the most optimal or efficient protocol will be investigated in future work.

For the protocol that we use, we can estimate the probability of the $|0\rangle$ state preparation failing, denoted $\epsilon_0$, as:

$$\epsilon_0 = n_{\text{th}}^{(c)} \cdot P(\text{“0”}|\,|1\rangle)^6 + (1 - n_{\text{th}}^{(c)}) \cdot [(1 - P(\text{“1”}|\,|0\rangle))^6 \cdot n_{\text{th}}^{(c)} \frac{2\, t_M}{T_1^{(c)}}]$$

where $P(\text{“}\alpha\text{”}|\,|\beta\rangle)$ denotes the probability of assigning the outcome “$\alpha$” conditioned on being in the state $|\beta\rangle$ (see Error Budget section for more detail), and the factor of 2 for the measurement time accounts for undetected cavity heating during the readout of the last cavity measurement, or the transmon check.

**Preparing the cavity in $|1\rangle$** In order to prepare the cavity in the $|1\rangle$ state, we first reset it to $|0\rangle$ as described for the prep $|0\rangle$ case. We then apply an OCP pulse as described in the Cavity-State Initialization section in order to initialize the cavity in $|1\rangle$, and append a transmon check as described in the Transmon Check section in order to confirm that the transmon is still in $|g\rangle$ following the initialization and before any subsequent operations to be performed on the qubit.

Represented in a circuit diagram, our prep $|1\rangle$ protocol is:

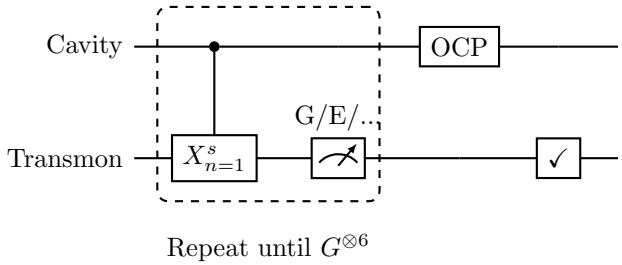


As emphasized in the Cavity-State Initialization section, there are many alternatives for initializing the cavity in $|1\rangle$, including sideband operations or measurement-based approaches. In addition, as described in [36], the state initialization (with any method) can followed by repeated cavity measurements in order to confirm the correct initialization and boost the preparation fidelity, termed "lucky-string" preparation. Alternative methods, as well as lucky-string preparation will be the topic of future work.

For the protocol that we use, we can estimate the probability of the $|1\rangle$ state preparation failing, denoted $\epsilon_1$, as:

$$\epsilon_1 = \epsilon_{ocp} + (1 - \epsilon_{ocp}) \cdot \frac{t_M}{T_1^{(c)}}$$

where $\epsilon_{ocp}$ denotes the OCP error, or the probability that it does not prepare the state $|1\rangle$.

In this work we assume that if the OCP fails the cavity is left in $|0\rangle$. In principle, there is also a probability that the cavity can be left in $|2\rangle$. While the probability of this occurring, and its effect on the logical space can be the topic of future work, we assume that this probability and its effect are small and neglect it in this work.

We monitored the OCP pulses of our subsystems on a weekly basis for three months prior to taking the data presented in this paper. Specifically, we performed quantum process tomography and extracted the X gate errors for each subsystem, shown in Fig. 7.

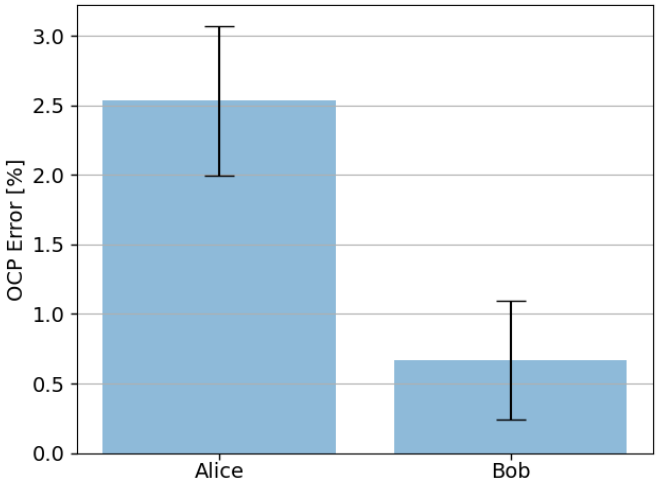


FIG. 7. The OCP error for initializing Alice (left) and Bob (right) in $|1\rangle$, extracted from QPT and averaged over three months prior to data. Error bars indicate the standard deviation.

**Preparing the Dual-Rail Basis States** In order to prepare any of the dual-rail basis states $\{|00\rangle, |01\rangle, |10\rangle, |11\rangle\}$ we simply simultaneously perform the relevant preparation operation as described above on each of the dual-rail's subsystems.

Using the expressions in each of the previous sections for $\epsilon_0$ and $\epsilon_1$, we can estimate our effective state preparation fidelities. We use our system parameters (see the System Properties section), and the OCP data shown in Fig. 7 to compute our estimates:

| | Alice | Bob |
|---|---|---|
| $\epsilon_0$ | $6.6 \times 10^{-7}$ | $2.0 \times 10^{-6}$ |
| $\epsilon_1$ | $2.5 \times 10^{-2}$ | $2.1 \times 10^{-2}$ |

As described previously, there are many alternative methods for dual-rail state preparation that can be explored in future work. In this work we opted for a simple state preparation protocol. This preparation protocol may not be the most optimal, and as such further demonstrates the utility of the dual-rail erasure detection to compensate for errors, including state preparation error, by flagging such errors as erasures.

In addition, using our estimates of the dual-rail state preparation fidelities together with our numerical model (see the Dual-Rail Measurement Numerical Simulations section for full detail), we find an anomaly in the agreement with the data in the cases where we prepare $|1_1\rangle$. Namely, while our model is physically-motivated and while we find good agreement with data across different experiments and protocols, we find that the model indicates that the $|1_1\rangle$ preparation fidelity is consistent with $\epsilon_1 = 5\times10^{-2}$ on Bob and $\epsilon_1 = 1\times10^{-3}$ on Alice – lower fidelities than we would estimate using our measured hardware properties. Again, this points to the opportunity in further investigation and optimization the state preparation in future work, indicating that yet further improvement in the dual-rail SPAM fidelity may be low-hanging fruit.

*Logical Measurement*

The protocol for the logical measurement of a dual-rail qubit that we have developed brings together most of the elements described in the cQED Toolbox for Bosonic Operations section in order to implement a measurement that is as robust as possible to the first-order errors, while taking into account the hierarchy of these first-order errors.

The logical measurements are first prepended by a transmon check to confirm that the logical measurement begins with the transmon in the ground state. This is especially important in our bit-flip and phase-flip experiments, where for long delay times between state preparation and measurement the transmon will most likely have thermalized and may be in the $|e\rangle$ state with around $\sim 1\%$ probability.

The logical measurement then consists of mapping the cavity-state to the transmon by way of a selective-pulse, followed by a transmon readout, a reset of the transmon back to $|g\rangle$ (conditioned on the readout outcome), and a post-reset transmon check to confirm that the transmon is in $|g\rangle$ after the reset. All as described above in the cQED Toolbox for Bosonic Operations section.

This post-reset check is intended to suppress the reset decision-making infidelity, that is limited by a readout classification error ($p_{miss}$) on the post-mapping measurement. Namely, in the case where we do not perform this check, if we perform an additional logical measurement it may begin with the transmon in $|e\rangle$ with probability $p_{miss}$ and lead to an incorrect outcome; in the case where we perform this post-reset check this will happen instead only with probability $p_{miss}^2$.

Represented in circuit diagrams form, our logical measurement consists of the following protocol, implemented simultaneously on each of the dual-rail's subsystems:

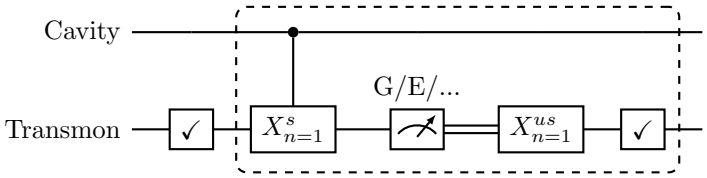


## SUPPLEMENTARY TEXT

### Dual-Rail Measurement Numerical Simulations

In order to numerically simulate the expected performance of the dual-rail cavity qubit and the expected outcomes of the characterization experiments, we developed a model for numerical simulation.

With this model we run QuTiP-based simulations [59, 60], that take the full set of independently-measured hardware parameters as input, and from which we extract the expected measurement outcome of the dual-rail qubit as output. Specifically, we perform a time-domain simulation of the dual-rail processes (delays, mapping, reset etc.) using QuTiP's master equation solver, and integrate this with our projective measurement model. Similar to the way in which we treat the measured dual-rail outcomes, the simulated readout outcomes are then correlated and histogrammed; this allows us to simulate and analyze any number of rounds of measurements, as well as simulating

and extracting the underlying quantum state in the hypothetical case of no measurement errors.

The main feature of the model is the way in which we model the transmon readout. In the dual-rail measurement protocol, after the the cavity state is mapped to the transmon, a dispersive readout is performed on the transmon.

Dispersive readout is a continuous process in which a probe tone is sent through the readout resonator, and the discrete state of the transmon is effectively mapped to the transmitted microwaves due to the transmon state-dependent frequency shift of the resonator [58]. In a transmon readout, it is nominally the $\sigma_z$ operator, or observable that is measured, and as such the readout "projects" the transmon state to one of the $\sigma_z$ eigenstates i.e. one of the computational basis states. In the dual-rail measurement protocol, the cavity state is always mapped to one of the transmon's computational basis states (i.e. $|g\rangle$ or $|e\rangle$, not a superposition state). This means that in the case where the measurement is a high-fidelity, single-shot QND (quantum non-demolition) readout, the measurement outcome should correspond to the physical state of the transmon that was measured – and the transmon state should be left unchanged, as it was in an eigenstate of the measured operator.

However, in practice, transmon readout is an error-prone process. Non-idealities of the measurement are primarily introduced by two sources:

1. State transitions of the transmon during the finite-duration readout. Such transitions will lead to a recorded outcome that is incorrect w.r.t to either the transmon's true initial or final underlying state. If the transmon undergoes a state transition event during the measurement, the assigned state w.r.t the transmon's initial state has some uncertainty. If the transition happens at an early point in the readout, then the transmon will be in the post-transition state for the majority of the readout time, and as such the assigned state will most likely reflect the transmon's post-readout state, and not its pre-readout state. Conversely, if the transition occurs closer to the end of the readout then the pre-transition state would already mostly have been mapped and the assigned state will most likely reflect the transmon's pre-readout state, but not its final post-readout state. Readout errors due to transmon state transitions are somewhat enhanced due to the increase in the transmon's thermal population during readout, and the decrease in its $T_1$ during readout [54].

2. Classification errors due to insufficient separation of the readout peaks in the IQ plane.

These two distinct sources of error motivate the way in which we model and implement the transmon readout in our model, and we handle these two sources of error separately. We do this since a number of components of the dual-rail protocol are conditioned on the transmon readout outcome, and we want to be able to separate the assigned measurement outcome (G/E) from the underlying state ($|g\rangle/|e\rangle$) that undergoes subsequent evolution in the protocol. In particular we want to capture the cases where the assigned state does not agree with the underlying state, and the ways in which this propagates and limits the performance of the overall protocol.

Specifically, in our modelling of the measurement we handle these two sources as follows. First we freely evolve the density matrix of the initial state $\rho_i$ for half the measurement duration time, $t_M$, using a generalized amplitude damping Kraus map to account for state transitions [61], we then apply "imperfect" measurement projectors (that account for the probability of classification errors) for each of the $j$ possible measurement outcomes, and then apply the Kraus map for then second half of $t_M$ to each of the projected states to account for the remaining transition probabilities and give us the final states $\rho_{f|j}$. $\rho_{f|j}$ is the density matrix of the final state, given that outcome $j$ was measured, where $\sum_j$ equals the number of possible measurement outcomes. For a more conceptual description see Fig. 8. We apply the measurement operators to the states mid-way through the measurement time (as opposed to at the beginning or the end) as a heuristic for the average probabilistic effect on the projected outcome, given the fact that a transmon transition can occur at any point during the measurement (as described in point 1 above).

The generalized amplitude damping Kraus map that we use was chosen in order to account for both heating and decay events in each of the dual-rail's modes during the readout time, and consists of the following operators:

$$K_0(t) = \sqrt{1-n_{th}}\ (\ |0\rangle\langle 0| + \sqrt{1-p_\downarrow(t)}\ |1\rangle\langle 1|\ )$$

$$K_1(t) = \sqrt{p_\downarrow(t)\ (1-n_{th})}\ |0\rangle\langle 1|$$

$$K_2(t) = \sqrt{n_{th}}\ (\ (1-p_\downarrow(t))\ |0\rangle\langle 0| + |1\rangle\langle 1|\ )$$

$$K_3(t) = \sqrt{p_\downarrow(t)\ n_{th}}\ |1\rangle\langle 0|$$

where $n_{th}$ is the mode's thermal population, $p_\downarrow = 1 - e^{-t/T_1}$ is the probability of decay of the mode's excited state, and $|0\rangle$ ($|1\rangle$) denotes the ground (excited) state of the mode (sub $|g\rangle$ and $|e\rangle$ in the case where the mode is one of the

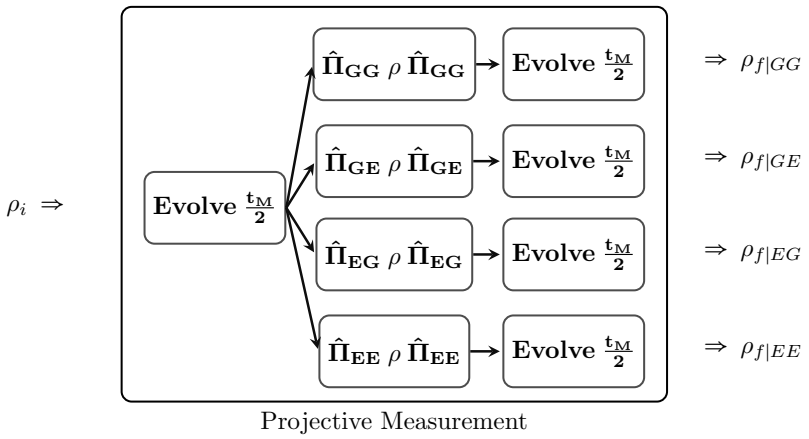


FIG. 8.

transmons). The map is then constructed and applied as

$$\mathcal{A}(\rho)(t) = \sum_{i=0}^{3} K_i(t)\rho K_i^\dagger(t)$$

In order to account for transitions in each of the four dual-rail's modes (the two cavities and two transmons) during the readout, we tensor four such Kraus maps where the cavities' maps take the measured $n_{th}^{(c)}$ and $T_1^{(c)}$, and the transmons' maps take the $n_{th\,RO}^{(t)}$ and $T_{1\,RO}^{(t)}$ values measured during readout.

The "imperfect" measurement projectors we use are constructed such as to form positive operator-valued measurements (POVM) elements that take classification errors into account as follows. In general, given the probabilities of misassigning $|g\rangle$ as $E$ (denoted as $p_{gE}$) or $|e\rangle$ as $G$ (denoted as $p_{eG}$), the assignment probability matrix is:

$$M = \begin{pmatrix} 1-p_{gE} & p_{eG} \\ p_{gE} & 1-p_{eG} \end{pmatrix}$$

In order to construct the corresponding set of POVMs, since each measurement will yield some outcome, we want to construct a complete set of $m$ projectors $\hat{\Pi}_m$, such that $\sum_m \hat{\Pi}_m^\dagger \hat{\Pi}_m = \mathbb{1}$ [62]. The ideal projectors would be

$$\hat{\Pi}_G = \begin{pmatrix} 1 & 0 \\ 0 & 0 \end{pmatrix}, \quad \hat{\Pi}_E = \begin{pmatrix} 0 & 0 \\ 0 & 1 \end{pmatrix}$$

As such, from the measurement outcome probabilities we can see that we can construct "imperfect" projectors that satisfy the completeness requirement, and are consistent with the zero-error limit as:

$$\hat{\Pi}_G = \begin{pmatrix} \sqrt{1-p_{gE}} & 0 \\ 0 & \sqrt{p_{eG}} \end{pmatrix}, \quad \hat{\Pi}_E = \begin{pmatrix} \sqrt{p_{gE}} & 0 \\ 0 & \sqrt{1-p_{eG}} \end{pmatrix}$$

or concisely, in general as $\hat{\Pi}_m = \sum_{i=0}^{d-1} \sqrt{M_{mi}}\,|i\rangle\langle i|$.

The projectors for the two-transmon dual-rail readout are constructed from these as:

$$\hat{\Pi}_{GG} = \mathbb{1} \otimes \hat{\Pi}_G \otimes \mathbb{1} \otimes \hat{\Pi}_G$$

$$\hat{\Pi}_{GE} = \mathbb{1} \otimes \hat{\Pi}_G \otimes \mathbb{1} \otimes \hat{\Pi}_E$$

$$\hat{\Pi}_{EG} = \mathbb{1} \otimes \hat{\Pi}_E \otimes \mathbb{1} \otimes \hat{\Pi}_G$$

$$\hat{\Pi}_{EE} = \mathbb{1} \otimes \hat{\Pi}_E \otimes \mathbb{1} \otimes \hat{\Pi}_E$$

where we tensor the transmon POVMs with the identity matrix on each of the cavities, and use independently-measured values of $p_{gE}$ and $p_{eG}$ for each of the two transmons projectors.

Conditioned on the projected outcome, we simulate additional components of the protocol. In the case of a transmon check, we only propagate forward the state $\rho_{f|GG}$, as this corresponds to the density matrix with the probabilistic distributions of the case where both transmons would get assigned as $G$ and "pass" the check. In the case of a conditional transmon reset, for any of the projected outcomes $\rho_{f|GE}$, $\rho_{f|EG}$, $\rho_{f|EE}$ we apply an unselective pi-pulse to the transmon mode that was projected to $E$.

In order to perform such unselective pulses, as well as selective pulses (for the cavity-state mapping), and logical dual-rail gates for the purpose of simulating the bit-flip and phase-flip experiments, we use functions native to the QuTiP wrapper package Sequencing [63].

### Error Budget for the Dual-Rail Measurement

In tandem with the numerical simulations, we have also developed an error budget "model" that provides us with a tool to perform analysis on contributing and limiting error channels in a different way. Namely, the error budget model is constructed in such a way that it takes all first-order error mechanisms of the dual-rail SPAM protocol into account, and provides us with the functional form of the individual error channels that contribute to the experimentally-measured SPAM outcomes. This provides us with a simple tool to: understand the scaling of the individual errors as a function of our particular hardware parameters, to quantify the relative contribution of various errors w.r.t each other, and to optimize the implementation of our protocol within the parameter space available to us.

The dual-rail qubit is encoded using multiple physical modes (namely two coupled bosonic modes), but is logically processed in a way that is different to a standard repetition code that might similarly be encoded in multiple physical modes. In the dual-rail encoding, the standard logical errors that we are interested in (Pauli errors, leakage etc.) now acquire contributions from multiple physical modes, and as such, the ways in which the underlying physical error mechanisms propagate and manifest in the space of the error-detected logical qubit are quite novel.

A convenient metric for quantifying the dual-rail performance is the SPAM matrix:

$$\hat{M} = \begin{pmatrix} p\left(\text{“00”} \mid \left|\tilde{00}\right\rangle\right) & p\left(\text{“00”} \mid \left|\tilde{10}\right\rangle\right) & p\left(\text{“00”} \mid \left|\tilde{10}\right\rangle\right) & p\left(\text{“00”} \mid \left|\tilde{11}\right\rangle\right) \\ p\left(\text{“01”} \mid \left|\tilde{00}\right\rangle\right) & p\left(\text{“01”} \mid \left|\tilde{01}\right\rangle\right) & p\left(\text{“01”} \mid \left|\tilde{10}\right\rangle\right) & p\left(\text{“01”} \mid \left|\tilde{11}\right\rangle\right) \\ p\left(\text{“10”} \mid \left|\tilde{00}\right\rangle\right) & p\left(\text{“10”} \mid \left|\tilde{01}\right\rangle\right) & p\left(\text{“10”} \mid \left|\tilde{10}\right\rangle\right) & p\left(\text{“10”} \mid \left|\tilde{11}\right\rangle\right) \\ p\left(\text{“11”} \mid \left|\tilde{00}\right\rangle\right) & p\left(\text{“11”} \mid \left|\tilde{01}\right\rangle\right) & p\left(\text{“11”} \mid \left|\tilde{10}\right\rangle\right) & p\left(\text{“11”} \mid \left|\tilde{11}\right\rangle\right) \end{pmatrix} \tag{1}$$

which is the matrix form of the sixteen measurement mapping outcomes presented in Fig. 2, and comprehensively quantifies the SPAM errors in the dual-rail space.

As it is an assignment matrix, if our SPAM were perfect $\hat{M}$ would be the identity matrix. As such, in order to understand our errors, the method of the error budget model is to decompose each of the twelve off-diagonal matrix element probabilities (the error elements) into its first-order contributing physical mechanisms. To do this, we decompose each outcome into its subsystems, e.g.:

$$p(\text{“00”} \mid |\tilde{10}\rangle) = p(\text{“0”} \mid |\tilde{1}\rangle)_{\mathrm{B}} \otimes p(\text{“0”} \mid |\tilde{0}\rangle)_{\mathrm{A}}$$

Under this decomposition of each of the matrix elements, it is clear that all of the matrix elements can in fact be computed from all the possible combinations (for each of the two subsystems) of just two error budgets:

1. $p(\text{“0”} \mid |\tilde{1}\rangle)_i$: Probability of assigning subsystem $i$'s cavity state to be "0", given that we tried to prepare it in $|1\rangle$.

2. $p(\text{“1”} \mid |\tilde{0}\rangle)_i$: Probability of assigning subsystem $i$'s cavity state to be "1", given that we tried to prepare it in $|0\rangle$.

In some cases of the error budget decomposition we will be interested in the probability of assigning a certain outcome conditioned on already being in a certain state. This is equivalent to ideal state preparation (i.e. the case where we are initially in a given state with unit probability), and we denote this case by removing the tilde on the prepared or initial state as $p(\text{“0”} \mid |1\rangle)_i$ and $p(\text{“1”} \mid |0\rangle)_i$. Using this method, in the model we can effectively "decouple" the state preparation errors from the measurement errors.

We develop this as a first-order model, by which we mean two things. First, we do not treat the cases of $p(\text{“0”}|\,|\tilde{0}\rangle)$ and $p(\text{“1”}|\,|\tilde{1}\rangle)$ – as there is no first-order (single-error) way for such outcomes to occur. Second, the error expressions for each step in the protocol are constructed such that they would lead to the outcome we are computing – if it were true that no errors occurred in any of the previous steps. It is important to note that we are considering only first-order errors in *each of the subsystems*, therefore when we consider the logical bit-flip case this is of course second order in the dual-rail space, but still analyzed considering only first order error contributions from each of the subsystems.

In addition to the system parameters defined in the System Properties section, we define the following parameters:

| **Parameter** | **Description** |
|---|---|
| $\epsilon_0$ | Probability of an error in preparing the cavity in $\|0\rangle$.<br>Given our state preparation protocol, the functional form of this error is<br>$\epsilon_0 = n_{th}^c \cdot P(\text{“0”}\,|\,|1\rangle) + (1 - n_{th}^c)[(1 - P(\text{“1”}\,|\,|0\rangle)) \cdot \frac{n_{th}^c t_M}{T_1^c}]$<br>i.e. limited by the cases where the cavity is excited but misassigned as “0”,<br>or where the cavity is in the ground state but heats during the transmon<br>check measurement. |
| $\epsilon_1$ | Probability of an error in preparing the cavity in $\|1\rangle$.<br>Given our state preparation protocol, the functional form of this error is<br>$\epsilon_1 = \epsilon_{ocp} + (1 - \epsilon_{ocp}) \cdot \frac{t_M}{T_1^c}$<br>i.e. limited by the cases where the OCP pulse initializing $\|1\rangle$ failed ($\epsilon_{ocp}$),<br>or where the initialization succeeded but the cavity relaxed during<br>the transmon check measurement. |
| $t_{map}$ | Duration of cavity-state mapping.<br>Implemented with a truncated Gaussian selective $\pi$-pulse, therefore equals $4\sigma_s$ |
| $t_{reset}$ | Duration of transmon reset.<br>Implemented with a truncated Gaussian unselective $\pi$- pulse, therefore equals $4\sigma_{us}$ |
| $p_{us}$ | Probability of an unselectivity error on the selective pulse.<br>Taking $\chi$ and $\sigma_s$ into account, it is computed numerically<br>as $Err = 1 - \|\langle 1, g\|X_{n=0}^s\|1, g\rangle\|^2$. |
| $p_s$ | Probability of a selectivity error on the unselective pulse.<br>Taking $\chi$ and $\sigma_{us}$ into account, it is computed numerically<br>as $Err = 1 - \|\langle 1, e\|X_{n=0}^{us}\|1, g\rangle\|^2$ |

The particular protocol considered is the following protocol for state preparation and measurement (as described in the State Preparation and Measurement Protocols section), where the circuit describes the protocol on one of the dual-rail's subsystems. State preparation followed by $M$ logical measurements with a transmon check before the logical measurements:

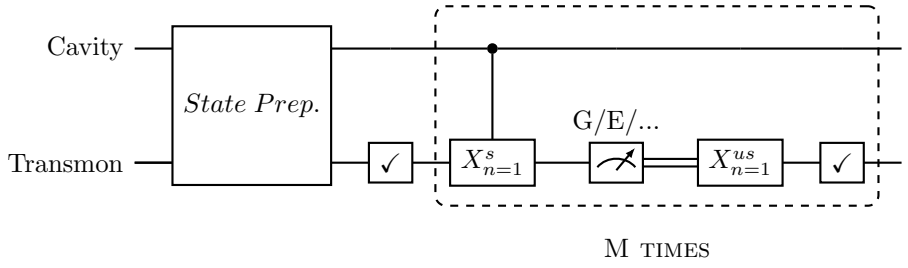


In this paper we concentrate on state preparation and single-measurement. Only processes that occur until the end of the first post-mapping transmon measurement are reflected in the outcome of this first logical measurement. Therefore, we consider only the following section of the protocol for the state preparation and single-measurment error budget:

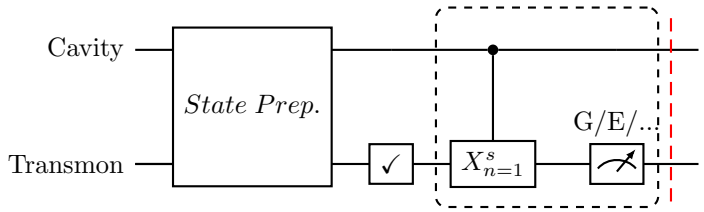


Logical Measurement

The error budgets (for the case where we also account for the state preparation i.e. SPAM) can then be constructed as follows:

1. $p(\text{“0”}|\,|\tilde{1}\rangle)$ Error Budget:

| | **Error Mechanism** | **Parameterization** |
|---|---|---|
| (1) | Prep 1 failure | $\epsilon_1$ |
| (2) | Cavity decay during transmon check or first half of cavity-state mapping | $\frac{2\,t_M+t_{map}}{2\,T_1^{(c)}}$ |
| (3) | $T_2$ event on transmon during cavity-state mapping | $\frac{t_{map}}{T_{2R}^{(t)}}$ |
| (4) | Transmon decay during first half of readout | $\frac{t_M}{2\,T_{1\,RO}^{(t)}}$ |
| (5) | Readout classification error | $p_{miss}$ |

2. $p(\text{“1”}|\,|\tilde{0}\rangle)$ Error Budget:

| | **Error Mechanism** | **Parameterization** |
|---|---|---|
| (1) | Prep 0 failure | $\epsilon_0$ |
| (2) | Cavity heating during transmon check, or first half of cavity-state mapping | $\frac{n_{th}^{(c)}(2\,t_M+t_{map})}{2\,T_1^{(c)}}$ |
| (3) | Transmon heating during second half of cavity-state mapping | $\frac{n_{th}^{(t)}\,t_{map}}{2\,T_1^{(t)}}$ |
| (4) | Transmon heating during first half of readout | $\frac{n_{th\,RO}^{(t)}\,t_M}{2\,T_{1\,RO}^{(t)}}$ |
| (5) | Unselectivity of selective pulse erroneously rotating the transmon | $p_{us}$ |
| (6) | Readout classification error | $p_{miss}$ |

Since we choose to account only for first-order events in this model, we make the assumption that there are no correlations between the errors–as any such correlation would be second-order–and therefore compute the probability of the expected outcome by simply summing the terms in the error budget.

For instance, for each of the three error events that we care about: *erasure* assignments, *leakage detection error* assignments, and *logical SPAM error* assignments, we construct the error budget as:

- Erasure:

$$\begin{aligned} p(\text{“00”}|\,|\tilde{01}\rangle) &= p(\text{“0”}|\,|\tilde{0}\rangle)_B \cdot p(\text{“0”}|\,|\tilde{1}\rangle)_A \\ &= (1-\sum_{i=1}^{6}[\,p(\text{“1”}|\,|\tilde{0}\rangle)\text{ Budget }]_B^{(i)}) \cdot (\sum_{i=1}^{5}[\,p(\text{“0”}|\,|\tilde{1}\rangle)\text{ Budget }]_A^{(i)}) \end{aligned}$$

- Leakage-Detection Error:

$$\begin{aligned} p(\text{“10”}|\,|\tilde{00}\rangle) &= p(\text{“1”}|\,|\tilde{0}\rangle)_B \cdot p(\text{“0”}|\,|\tilde{0}\rangle)_A \\ &= (\sum_{i=1}^{6}[\,p(\text{“1”}|\,|\tilde{0}\rangle)\text{ Budget }]_B^{(i)}) \cdot (1-\sum_{i=1}^{6}[\,p(\text{“1”}|\,|\tilde{0}\rangle)\text{ Budget }]_A^{(i)}) \end{aligned}$$

- Logical SPAM Error:

$$p(\text{“10”}|\,|\tilde{01}\rangle) = p(\text{“1”}|\,|\tilde{0}\rangle)_B \cdot p(\text{“0”}|\,|\tilde{1}\rangle)_A$$
$$= (\sum_{i=1}^{6}[\; p(\text{“1”}|\,|\tilde{0}\rangle)\text{ Budget }]_B^{(i)}) \cdot (\sum_{i=1}^{5}[\; p(\text{“0”}|\,|\tilde{1}\rangle)\text{ Budget }]_A^{(i)})$$

Similarly, we can construct the error budget for all other dual-rail SPAM error outcomes. In the next two subsections we show two ways in which we can use the error budget formalism to analyze the individual contributions of various error mechanism to our measured dual-rail performance.

*Breakdown of SPAM Error*

One immediate application of the error budget is to breakdown the each of the SPAM error-outcomes to its contributing factors. Namely, we can focus on the SPAM experiment described in the Characterizing dual-rail SPAM section where we prepare all four joint cavity states in turn and then measure the probabilities of assigning each of the four possible joint cavity states. In this experiment there are twelve error outcomes, or the twelve off-diagonal elements of the corresponding SPAM matrix (see eqn. 1).

As established in this paper, our measured dual-rail outcomes have contributions both from the intrinsic hardware coherences as well as from errors introduced by the protocols of the state preparation and measurement. With an eye towards future work on hardware and protocol optimization in order to improve the dual-rail cavity qubit's performance, we show the error breakdown of the six most important SPAM error terms, in three groups, as an initial guide to where such work would ideally first be focused.

Specifically, the three error groups that we care about are erasure assignments, where we prepare a logical state and it gets assigned to “00” (see Table I); leakage detection error assignments, where the leakage state $|00\rangle$ gets assigned to one of the logical states “01” or “10” (see Table II); and logical SPAM errors, where one of the logical states gets assigned to the other logical state (see Table III). For the bit-flip SPAM outcome we quote only the top five error contributions.

From our error analysis we notice two things. First, we see that the particular values of the hardware parameters of each of the dual-rail's subsystems give rise to very different relative error contributions. In other words, for example, a “00” assignment having prepared $|\tilde{01}\rangle$ as opposed to $|\tilde{10}\rangle$ will have a different error budget. This is important to understand, particularly for the case of logical Pauli errors, as these are second-order error that will therefore occur due to error contributions from both subsystems.

Second, our analysis quantifies and emphasizes that as expected, actual cavity transitions are not the dominant error source. Instead, our SPAM errors are dominated by ancillae transmon errors. *Erasure* assignments (Table I) where a prepared logical state gets assigned as an erasure, both get very significant contributions ($30\% - 50\%$) from transmon decay events during the readout; *leakage detection error* assignments (Table II) are dominated by transmon readout classification errors (60%-90%); and a dominant contribution to *logical SPAM error* assignments (Table III) is the combination of these errors on each subsystem ($\sim 30\%$).

*Breakdown of Bit-Flip Error*

The logical lifetime of the dual-rail cavity qubit is characterized using the bit-flip experiment as described in the Measuring Bit-Flip Errors section. We know that the intrinsic physical mechanism of the logical bit flip is dominated by the rare case of a double transition event: a decay in the cavity prepared in $|1\rangle$ *and* a heating event in the cavity prepared in $|0\rangle$. However, in the process of measuring the dual-rail's state in order to characterize its bit-flip time – many more errors are introduced. These state-mapping and measurement errors result in an “effective”, or “measured” bit-flip rate that is much faster than the estimated intrinsic bit-flip rate that is solely due to double cavity transitions.

In order to better understand and support this distinction between the “measured” bit-flip and the “intrinsic” bit-flip, we can use our models to construct an error budget of the relative contributions to each of the bit-flip rates.

TABLE I. ***Erasure*** **Assignments**

| **Error Outcome** | **Error Description** | **Raw Contribution** | **Relative Contribution** |
|---|---|---|---|
| $p(\text{“00”}\|\|\widetilde{01}\rangle)$ | Transmon $T_1$ during readout | 2.77e-2 | 47.75% |
| | Transmon $T_2$ during mapping | 1.24e-2 | 21.36 % |
| | State ($\|1\rangle$) preparation failure | 9.26e-3 | 15.99 % |
| | Cavity $T_1$ during check or mapping | 4.6e-3 | 7.94 % |
| | Readout classification error | 4.03e-3 | 6.96 % |
| $p(\text{“00”}\|\|\widetilde{10}\rangle)$ | State ($\|1\rangle$) preparation failure | 2.84e-2 | 40.73 % |
| | Transmon $T_1$ during readout | 2.18e-2 | 30.40 % |
| | Cavity $T_1$ during check or mapping | 1.21e-2 | 17.37 % |
| | Transmon $T_2$ during mapping | 6.82e-3 | 9.80 % |
| | Readout classification error | 1.18e-3 | 1.69 % |

TABLE II. ***Erasure conversion error*** **assignments**

| **Error Outcome** | **Error Description** | **Raw Contribution** | **Relative Contribution** |
|---|---|---|---|
| $p(\text{“01”}\|\|\widetilde{00}\rangle)$ | Readout classification error | 3.14e-3 | 89.05 % |
| | Transmon heating during readout | 2.771e-4 | 7.86 % |
| | State ($\|0\rangle$) preparation failure | 5.48e-5 | 1.56 % |
| | Transmon heating during mapping | 4.60e-5 | 1.30 % |
| | Cavity heating during check or mapping | 4.60e-6 | 0.13 % |
| | Unselectivity of selective mapping pulse | 3.75e-6 | 0.10% |
| $p(\text{“10”}\|\|\widetilde{00}\rangle)$ | Readout classification error | 3.22e-3 | 58.90 % |
| | Transmon heating during readout | 2.12e-3 | 38.74 % |
| | State ($\|0\rangle$) preparation failure | 6.39e-3 | 1.17 % |
| | Transmon heating during mapping | 3.54e-5 | 0.65 % |
| | Unselectivity of selective mapping pulse | 1.75e-5 | 0.32 % |
| | Cavity heating during check or mapping | 1.21e-5 | 0.22 % |

The probabilities of measuring a logical bit-flip, when preparing $0_\text{L}$ or $1_\text{L}$ are defined as, respectively

$$P_{1_\text{L}}(t) = \frac{P(m_{10}(t)|\text{ prep } 01)}{P(m_{10}(t)|\text{ prep } 01) + P(m_{01}(t)|\text{ prep } 01)}$$

$$P_{0_\text{L}}(t) = \frac{P(m_{01}(t)|\text{ prep } 10)}{P(m_{10}(t)|\text{ prep } 10) + P(m_{01}(t)|\text{ prep } 10)}$$

where $m_{01}$ and $m_{10}$ are the raw probabilities of assigning the states “01” and “10” (i.e before re-normalization of the logical subspace), and are given by the sum of the probabilities of assigning the outcome “01” or “10” (denoted $\mathcal{O}$ in general) conditioned on being in any one of the dual-rail states $|k\rangle$:

$$m_{\mathcal{O}}(t) = \sum_{k\in\{|00\rangle,|01\rangle,|10\rangle,|11\rangle\}} P_{|k\rangle}(t) \;\cdot\; P\left(\mathcal{O} \mid |k\rangle\right) \tag{2}$$

By solving a simple system of ODEs we can obtain each of the $P_{|k\rangle}(t)$ terms of the **dual-rail state evolutions** in eqn. 2, and using our model we can compute each of the $P\left(\mathcal{O} \mid |k\rangle\right)$ terms of the **assignment probabilities** in eqn. 2. In this case when we compute the assignment probabilities we do not include state preparation errors, since we are conditioning the outcomes on already being in each of the dual-rail states.

TABLE III. ***Logical SPAM error*** **assignments**

| **Error Outcome** | **Error Description** | **Raw Contribution** | **Relative Contribution** |
|---|---|---|---|
| $p(\text{“10”}\|\|\tilde{01}\rangle)$ | Readout classification error (B) and Transmon $T_1$ during readout (A) | 8.91e-5 | 28.13 % |
| | Transmon heating during readout (B) and Transmon decay during readout (A) | 5.86e-5 | 18.50 % |
| | Readout classification error (B) and Transmon $T_2$ during mapping (A) | 3.98e-5 | 12.58 % |
| | Transmon heating during readout (B) and Transmon $T_2$ during mapping (A) | 2.62e-5 | 8.27 % |
| | Transmon heating during readout (B) and State ($\|1\rangle$) preparation failure (A) | 1.96e-5 | 6.19 % |
| $p(\text{“01”}\|\|\tilde{10}\rangle)$ | State ($\|1\rangle$) preparation failure (B) and Readout classification error (A) | 8.90e-5 | 36.27 % |
| | Transmon $T_1$ during readout (B) and Readout classification error | 6.64e-5 | 27.07 % |
| | Cavity $T_1$ during check or mapping (B) and Readout classification error (A) | 3.79e-5 | 15.47 % |
| | Transmon $T_2$ during mapping (B) and Readout classification error (A) | 2.14e-5 | 8.73 % |
| | State ($\|1\rangle$) preparation failure (B) and Transmon heating during readout (A) | 7.85e-6 | 3.20 % |
| | Transmon $T_1$ during readout (B) and Transmon heating during readout | 5.86e-6 | 2.39 % |

**Dual-Rail State Evolutions** As we are interested in the long-time behavior of the logical bit-flip, we solve the system of ODEs for the two-level cavity system in order to extract the exact expressions of the evolution of the ground and excited populations of the cavity states, and construct the expressions for the dual-rail state evolutions, $P_{|k\rangle}(t)$ from these.

Treating each cavity as a two-level system, the evolution of the ground and excited state populations can be expressed as the following system of ODEs:

$$\begin{pmatrix}\dot{P}_0\\ \dot{P}_1\end{pmatrix} = \begin{pmatrix}-\Gamma_\uparrow & \Gamma_\downarrow\\ \Gamma_\uparrow & -\Gamma_\downarrow\end{pmatrix}\begin{pmatrix}P_0\\ P_1\end{pmatrix} \tag{3}$$

where $\Gamma_\downarrow = 1/T_1$ and $\Gamma_\uparrow = n_{th}/T_1$.

Using the error budget we can compute the $|0\rangle$ and $|1\rangle$ state preparation errors: $\epsilon_0$ and $\epsilon_1$, with which we define the initial conditions for the ODEs. For the case where $|\psi_0\rangle = |\tilde{0}\rangle$: $\{P_0(0) = 1-\epsilon_0,\ P_1(0) = \epsilon_0\}$, and for the case where $|\psi_0\rangle = |\tilde{1}\rangle$: $\{P_0(0) = \epsilon_1,\ P_1(0) = 1-\epsilon_1\}$. Solving eqn. 3 with these initial conditions we find for the case where $|\psi_0\rangle = |\tilde{0}\rangle$:

$$P_{(0|\text{init }|0\rangle)}(t) = \frac{\Gamma_\downarrow}{\Gamma_\uparrow+\Gamma_\downarrow} + e^{-(\Gamma_\uparrow+\Gamma_\downarrow)t}\,(\frac{\Gamma_\uparrow}{\Gamma_\uparrow+\Gamma_\downarrow} - \epsilon_0)$$
$$P_{(1|\text{init }|0\rangle)}(t) = \frac{\Gamma_\uparrow}{\Gamma_\uparrow+\Gamma_\downarrow}\,(1-e^{-(\Gamma_\uparrow+\Gamma_\downarrow)t}) + \epsilon_0\,e^{-(\Gamma_\uparrow+\Gamma_\downarrow)t}$$

and for the case where $|\psi_0\rangle = |\tilde{1}\rangle$:

$$P_{(0|\text{init }|1\rangle)}(t) = \frac{\Gamma_\downarrow}{\Gamma_\uparrow+\Gamma_\downarrow}\,(1-e^{-(\Gamma_\uparrow+\Gamma_\downarrow)t}) + \epsilon_1\,e^{-(\Gamma_\uparrow+\Gamma_\downarrow)t}$$
$$P_{(1|\text{init }|1\rangle)}(t) = \frac{\Gamma_\uparrow}{\Gamma_\uparrow+\Gamma_\downarrow} - e^{-(\Gamma_\uparrow+\Gamma_\downarrow)t}(\epsilon_1 - \frac{\Gamma_\downarrow}{\Gamma_\uparrow+\Gamma_\downarrow})$$

With these solutions we can then construct the functional form of the evolution of the dual-rail cavity states as $P_{(|00\rangle|\text{init }|01\rangle)} = P^B_{(0|\text{init }|0\rangle)}(t)\cdot P^A_{(0|\text{init }|1\rangle)}(t)$ etc., where $\Gamma_\uparrow$ and $\Gamma_\downarrow$ for each cavity's solution are parameterized by the

cavity's measured $T_1$ and $n_{th}$. The result using our system's parameters are plotted in Fig. 9.

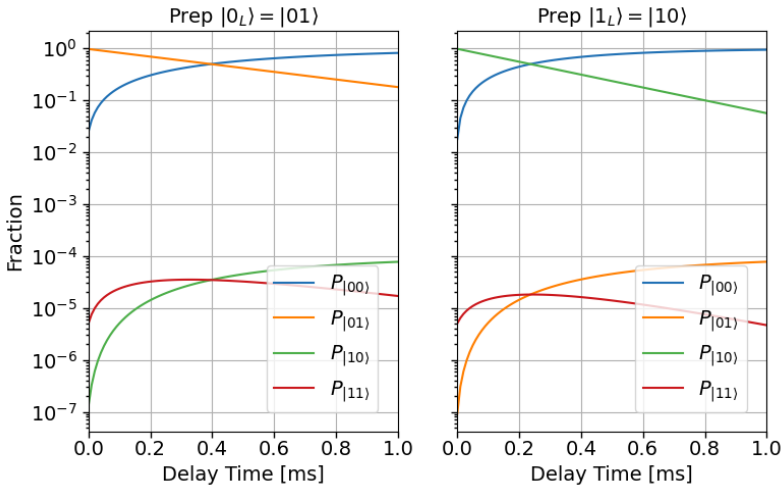


FIG. 9. Time evolution of the four dual-rail basis states over 1 ms, in the case where $|0_\mathrm{L}\rangle$ is prepared (left), and in the case where $|1_\mathrm{L}\rangle$ is prepared (right).

**Assignment Probabilities** Using our model, we can also compute the assignment probabilities conditioned on being in any one of the dual-rail states, $P(\mathcal{O} \mid |k\rangle)$. The results are plotted in Fig. 10.

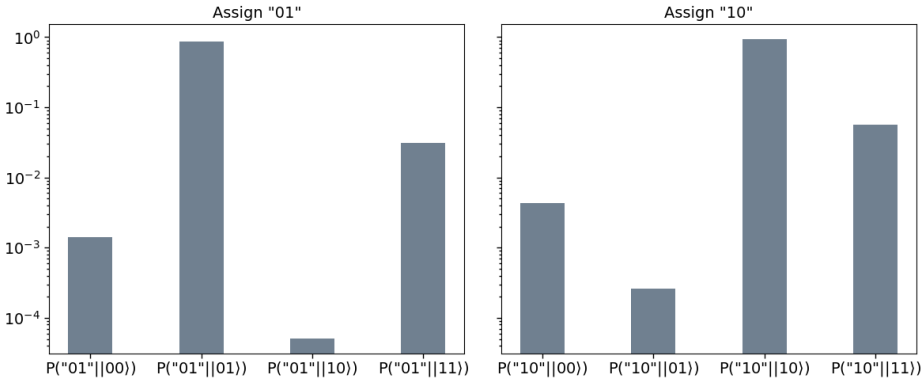


FIG. 10. Probability of assigning the logical basis outcomes–conditioned on being in each of the dual-rail basis states; computed using the error budget. The probability of assigning "01" from each of the basis states in plotted on the left, and the probability of assigning "10" from each of the basis states is plotted on the right.

These assignment probabilities are similar to the left two panels in Fig.2. However, as noted, in Fig.2 the numbers reflect the SPAM outcomes (including state preparation) whereas Fig. 10 reflects only the measurement errors, assuming perfect state preparation.

In general, we are most interested in using the model to quantify two things. We know that the measured bit-flip rate gets some contribution from the intrinsic bit-flip (a heating event on one cavity and a decay event on the other cavity), and some contribution from measurement errors introduced when trying to measure the bit-flip rate. We are interested then in:

1. Understanding what fraction of the measured bit-flip rate is due to the true intrinsic bit-flip.
2. For the measured bit-flip rate, which measurement assignment channel $P_{|k\rangle} \cdot P(\mathcal{O} \mid |k\rangle)$ dominates the measured outcome.

To answer these questions we single out the three cases of interest:

1. **Only intrinsic bit-flip**. The case where finite cavity $T_1$ and $n_{th}$ lead to real logical bit-flips at long delay times; we assume perfect measurements in order to isolate this mechanism.

   In the case where there is no measurement error, a logical state will only be measured if it is actually the underlying physical state, i.e. the measurement outcomes are:

   $$m_{01} = P_{|01\rangle}$$
   $$m_{10} = P_{|10\rangle}$$

   For delay times on the order of the bare cavity $T_1$s, we can approximately express the intrinsic logical bit-flip probabilities as

   $$P(\text{flip} \mid \text{initial } |0_L\rangle) = P_{1_L} = \frac{(1 - e^{-n_{th}t/T_1^{(B)}})(1 - e^{-t/T_1^{(A)}})}{(e^{-n_{th}t/T_1^{(B)}})(e^{-t/T_1^{(A)}}) + (1 - e^{-n_{th}t/T_1^{(B)}})(1 - e^{-t/T_1^{(A)}})}$$

   and

   $$P(\text{flip} \mid \text{initial } |1_L\rangle) = P_{0_L} = \frac{(1 - e^{-t/T_1^{(B)}})(1 - e^{-n_{th}t/T_1^{(A)}})}{(1 - e^{-t/T_1^{(B)}})(1 - e^{-n_{th}t/T_1^{(A)}}) + (e^{-t/T_1^{(B)}})(e^{-n_{th}t/T_1^{(A)}})}$$

   At short times, from first-order Taylor expansion we can extract the expression:

   $$P(\text{flip} \mid \text{initial } |0_L\rangle) = n_{th}^{(B)} \frac{t^2}{T_1^{(A)}\, T_1^{(B)}} = n_{th}^{(B)}\ \kappa_A\ \kappa_B\ t^2$$

   and

   $$P(\text{flip} \mid \text{initial } |1_L\rangle) = n_{th}^{(A)} \frac{t^2}{T_1^{(A)}\, T_1^{(B)}} = n_{th}^{(A)}\ \kappa_A\ \kappa_B\ t^2$$

   showing that at short times the intrinsic bit-flip is quadratic in time.

   At long times compared to the bare cavity $T_1$ we use the exact expressions for the population probabilities, which are reflected in the plots below.

2. **Only measurement error bit-flip**. In this case we set the cavity $n_{th}$ to zero, such that there can by no real intrinsic bit-flip, and the probability of assigning a bit-flip is only due to the measurement.

   This means that for the case where $|\psi_0\rangle = |1_L\rangle$:

   $$m_{01} = P_{|00\rangle} \cdot P(\text{“01”} |\ |00\rangle) + P_{|10\rangle} \cdot P(\text{“01”} |\ |10\rangle)$$

   $$m_{10} = P_{|00\rangle} \cdot P(\text{“10”} |\ |00\rangle) + P_{|10\rangle} \cdot P(\text{“10”} |\ |10\rangle)$$

   and for the case where $|\psi_0\rangle = |0_L\rangle$:

   $$m_{01} = P_{|00\rangle} \cdot P(\text{“01”} |\ |00\rangle) + P_{|01\rangle} \cdot P(\text{“01”} |\ |01\rangle)$$

   $$m_{10} = P_{|00\rangle} \cdot P(\text{“10”} |\ |00\rangle) + P_{|01\rangle} \cdot P(\text{“10”} |\ |01\rangle)$$

   from which, using the ODE solutions and the assignment probabilities, we can construct the functional form of the logical bit-flip in each case.

3. **Intrinsic bit-flip and measurement errors**. The realistic case where we have both finite cavity coherences and finite measurement errors.

   In the case where we allow for an intrinsic bit-flip, i.e. $n_{th} \neq 0$, as well as measurement errors, there is a probability of being in, or measuring any one of the four states. Therefore, we must account for all terms in eqn. 2. Again, substituting the appropriate expression for $P_{|k\rangle}$ and the assignment probabilities for each of the cases we then construct the functional form of the logical bit-flips.

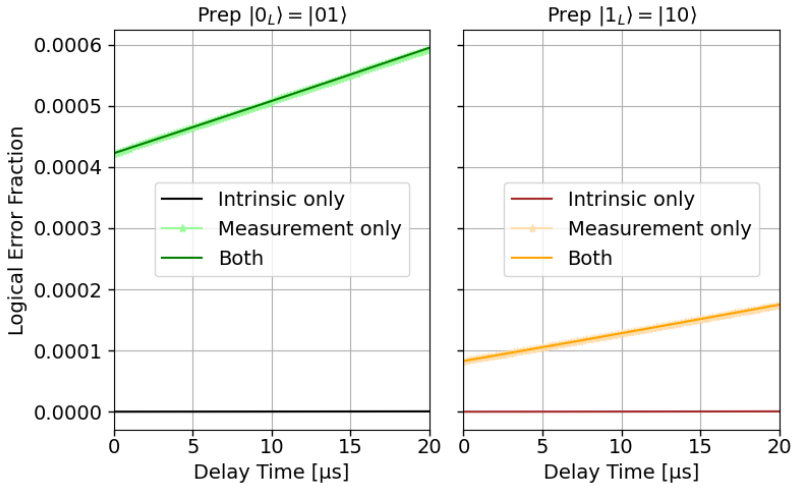


FIG. 11. Probability of a logical bit-flip from different error channels, given $|0_L\rangle$ preparation (left) and $|1_L\rangle$ preparation (right). *Intrinsic only* represents the case where measurements are perfect and therefore a bit-flip can only occur as a result of double-transitions; *measurement only* represents the case where the cavity $n_{th} = 0$, and therefore bit-flips are only apparent bit-flips due to measurement errors; *both* represents the case where both of these error channels are finite.

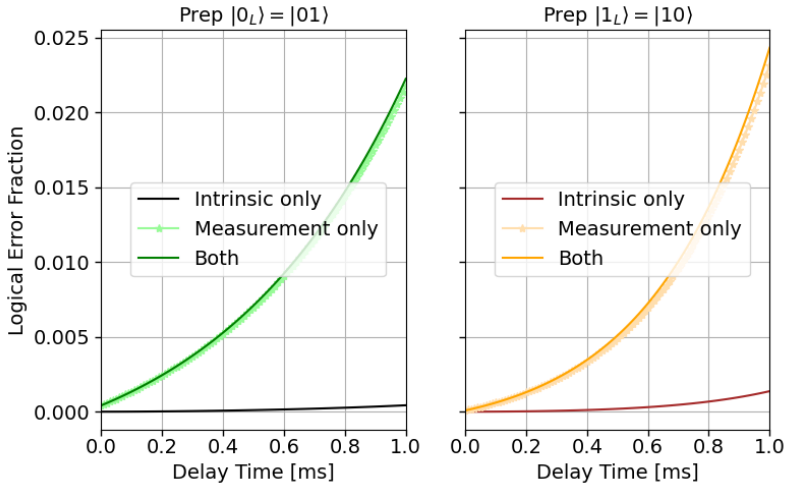


FIG. 12. Same as Fig. 11, but delayed out to 1 ms.

We can plot each of these three cases for the delay times of interest discussed in this paper: 20 $\mu$s and 1 ms. The results are presented in Fig. 11, and Fig. 12, respectively. In addition, we can plot the three cases for a delay time of 10 ms, longer than we measure, in order to observe the expected saturation of the logical bit-flip probability; the results are presented in Fig. 13.

The plots in Figures 11 and 12 show the extent to which the measured bit-flip probability is dominated by errors of the measurement itself, and not by the true intrinsic bit-flip. As described in the Measuring Bit-Flip Errors section, this shows why via measurement we can only bound the bit-flip rate to $1/(\sim 80$ ms), while given the cavity coherences we estimate the true intrinsic bit-flip rate is on the order of $1/(\sim 2.5$ s).

Specifically, we can now further use these computed state evolutions and assignment probabilities in order to answer our two initial questions.

First, the fraction that the intrinsic bit-flip constitutes of the total measured bit-flip probability is simply the "Measurement only" outcome plotted in Fig. 12, divided by the total measured bit-flip ("Both" in Fig. 12). This ratio, as a function of the delay time, is plotted in Fig. 14. As described in section , we bound the cavity thermal population to be between 1e-3 and 1e-4. Therefore, in Fig. 14 we plot this ratio for both values of cavity thermal population, in order to establish a the range that we expect this contribution to be in our case. For cavity thermal

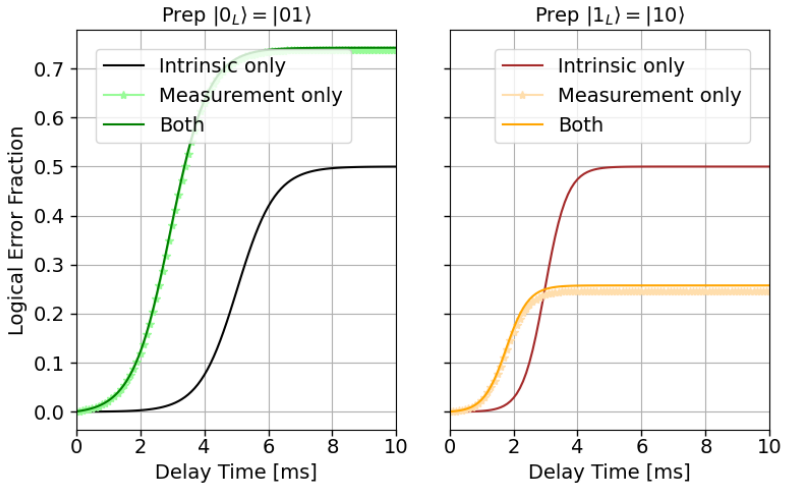


FIG. 13. Same as Fig. 11, but delayed out to 10 ms.

populations of $10^{-4}$, which is closer to what we measure, we learn from the model that the intrinsic bit-flip contributes $(0.04 - 0.13)\%$ at 1 $\mu$s, and $(1.93 - 5.64)\%$ 1 ms, where the range is given by the two state preparations.

Using the model we can also confirm our expectations of the contributions of the respective bit-flip channels at very long times compared to the cavity lifetimes. At these long times, the cavities will have thermalized, and we expect the intrinsic bit-flip for both initial state preparations to saturate to

$$\frac{n_{th} \cdot (1 - n_{th})}{n_{th} \cdot (1 - n_{th}) + (1 - n_{th}) \cdot n_{th}} = \frac{1}{2}$$

Similarly, at long times when the cavities have thermalized, we expect the contribution of the measurement error-induced bit-flip to be given by the ratio of the probabilities of misassigning $|00\rangle$ to each of the bit-flip outcomes:

$$P(\text{flip}|\text{initial } |0_\text{L}\rangle) = \frac{P(\text{“10”}||00\rangle)}{P(\text{“01”}||00\rangle) + P(\text{“10”}||00\rangle)}$$

$$P(\text{flip}|\text{initial } |1_\text{L}\rangle) = \frac{P(\text{“01”}||00\rangle)}{P(\text{“01”}||00\rangle) + P(\text{“10”}||00\rangle)}$$

From the logical state assignments that we compute using the model (see Fig. 10) we can extract these numbers and see that $P(\text{“10”}||00\rangle) = 4.26 \times 10^{-3}$, and $P(\text{“01”}||00\rangle) = 1.42 \times 10^{-3}$. Therefore we expect the logical bit-flip probability at long times to saturate to 0.75 for prep $|0_\text{L}\rangle$, and 0.25 for prep $|1_\text{L}\rangle$.

Both of these expectations are confirmed by the model, see Fig. 13.

Second, for the measured bit-flip rate, we can decompose the measured number into the contributions it gets from assigning each of the dual-rail states to the bit-flip outcome. We do this to answer our question about which of the assignment channels dominates the logical bit-flip, and to what extent.

Specifically, we decompose it as follows. As described in eqn. , the probability of a logical bit-flip outcome for the case where the initial state is $|0_L\rangle$ is given by

$$P_{1_L}(t) = \frac{P(m_{10}(t)|\text{ prep } 01)}{P(m_{10}(t)|\text{ prep } 01) + P(m_{01}(t)|\text{ prep } 01)}$$

We can write the numerator out explicitly, in which case

$$P_{1_L}(t) = \frac{P_{|00\rangle} \cdot P(\text{“10”}||00\rangle) + P_{|01\rangle} \cdot P(\text{“10”}||01\rangle) + P_{|10\rangle} \cdot P(\text{“10”}||10\rangle) + P_{|11\rangle} \cdot P(\text{“10”}||11\rangle)}{P(m_{10}(t)|\text{ prep } 01) + P(m_{01}(t)|\text{ prep } 01)}$$

Each term in this last expression can be interpreted as the contribution to the total measured bit-flip from the probability of assigning each of dual-rail states to the bit-flip outcome.

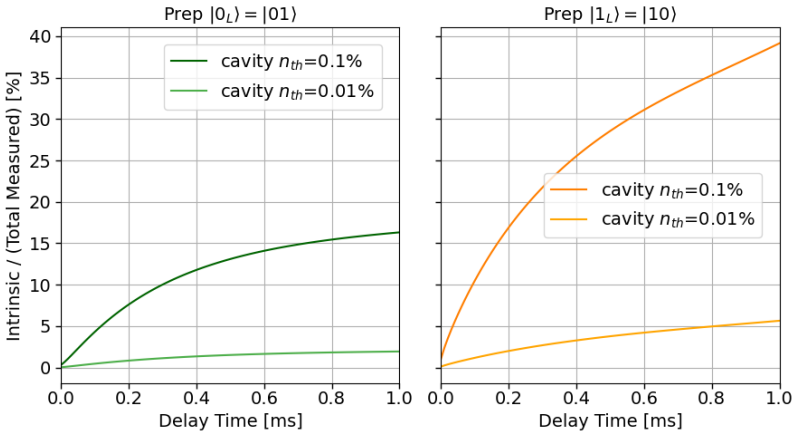


FIG. 14. Fraction that the intrinsic bit-flip contributes to the total measured bit-flip, for delay times up to 1 ms, given prep $|0_L\rangle$ (left) and $|1_L\rangle$ (right). Plotted both for cavity $n_{\text{th}}$ of 0.1% and 0.01%.

In Fig. 15 we plot the contribution of each of these bit-flip assignment channels, for each of the logical states. The sum of all these channels for each logical state corresponds to the bit-flip probability that we would measure; in Fig. 15 the data is overlaid with the model and we do indeed see good agreement.

From this plot we can see the extent to which the measured bit-flip outcome is dominated by misassignment of the leakage state $|00\rangle$ to the bit-flip outcome in the case of both logical states, where the measured probability can in fact be attributed almost entirely to this assignment channel. At 1 $\mu$s, the "$|00\rangle$ to bit-flip outcome" assignment channel contributes $\sim 34\%$ to the measured bit-flip probability, and at 1 ms it contributes $\sim 95\%$.

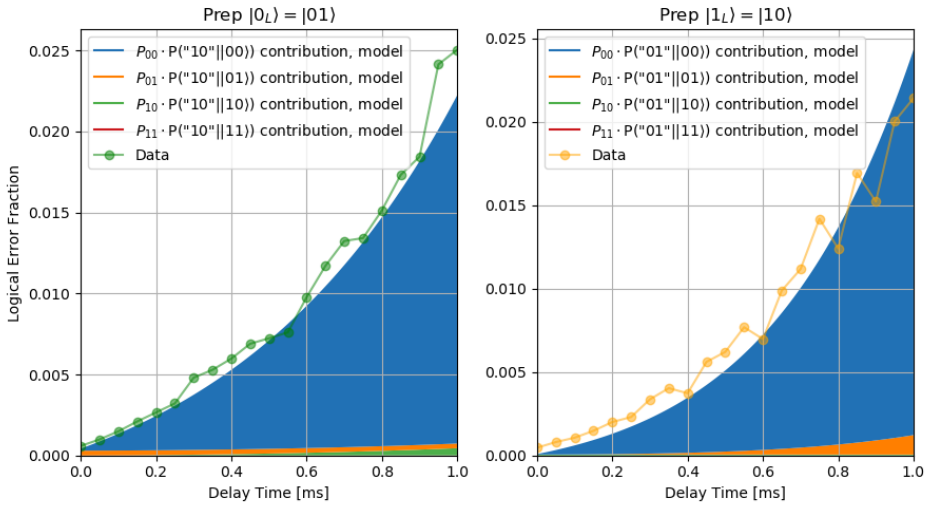


FIG. 15. The measured bit-flip probability gets contributions from each of the dual-rail basis states getting assigned to the bit-flip outcome. Here we plot each of these contributions in order to show the relative contributions of each assignment channel to the measured bit flip for prep $|0_L\rangle$ (left) and prep $|1_L\rangle$ (right). The sum of the contributions should correspond to the data.

### Intrinsic Bit-Flip Estimate

An important metric of the coherence of the logical qubit is the rate at which the logical basis states "flip" to the other logical state, resulting in an effective bit-flip. As described in the main text, we identify two primary contributions to this rate: "intrinsic" processes, and measurement-introduced processes. The combination of these processes result in the "apparent" bit-flip that we measure (see the Measuring Bit-Flip Errors section).

While we can place a measured, SPAM-limited bound on the bit-flip rate, we are also interested in extracting the intrinsic bit-flip rate as a figure of merit for our dual-rail qubit. The intrinsic bit-flip rate is the true idling bit-flip rate, and thus is the true rate applicable during any operation of the qubit in a circuit.

Specifically, there are two intrinsic processes that contribute to effective transitions between the logical states. First, there is a finite probability of actual double-transitions, where both photon-loss in one cavity and photon-gain in the other cavity occur and induce a flip in the logical state. Second, a difference in the cavity decay rates will cause evolution in the no-jump trajectory [2] toward the cavity with the longer lifetime, with the resulting backaction flipping the logical state.

Measurement errors contribute to the bit-flip rate when performing an experiment in order to measure the bit-flip rate. In this case non-bit-flip outcomes will get assigned to the bit-flip outcome as a result of measurement errors, and thus increase the apparent rate of the logical bit flips.

By way of measurement we have of course have no way of decoupling these measurement errors from the intrinsic errors in order to quantify each separately. However, in theory we know exactly what the contributions to the intrinsic processes are and as such, using our measured system parameters (see the System Properties section), we can compute the intrinsic bit-flip rate of our qubit.

*a. Leakage-seepage contribution*

From the functional form of the time evolution of the dual-rail states (see eqn. 3) given finite fidelity state-preparation, we can extract the probabilities of a leakage-seepage event at $1\mu s$ for each of the logical state preparation: $P_{(|01\rangle||10\rangle)}(t = 1\mu s)$ and $P_{(|10\rangle||10\rangle)}(t = 1\mu s)$, and extract a time constant from this as

$$T_{flip} = \frac{1\mu s}{P_{\text{leakage-seepage}}(t = 1\mu s)}$$

For our system's parameters we find that for prep $|0_\text{L}\rangle$ and $|1_\text{L}\rangle$ the qubit lifetime due to this bit-flip channel is $T_{\text{flip } |0_\text{L}\rangle\rightarrow|1_\text{L}\rangle} = 6.74\ s$ and $T_{\text{flip } |1_\text{L}\rangle\rightarrow|0_\text{L}\rangle} = 9.06\ s$.

*b. No-jump backaction contribution*

In the case where the lifetimes of each of the dual-rail's cavity are not the same ($T_1^A \neq T_1^B$), a dual-rail state with finite population in both of the logical states will be susceptible to the effect of the no-jump backaction [2, 36]. Under the no-jump evolution, conditioned on the case where no jump (decay event) occurs, the quantum amplitude of the logical state defined by an excitation in the longer-lived cavity will increase at the expense of the quantum amplitude of other logical state.

In the context of the bit-flip experiment where we try to initialize in a basis state, if the state preparation was perfect the no-jump backaction would have no effect as there would be no probability of being in the other logical state. However, in practice the fidelity of state-preparation will always be finite, and as such there will always be some small finite probability of being in an undesired ensemble state–vulnerable to the no-jump backation.

While no population transfer occurs due to this effect, and in that sense it is not comparable to a $\hat{\sigma}_x$ type bit-flip, under this deterministic evolution the relative amplitudes of the logical states will polarize towards the bit-flip-outcome, and then be measured as such what projecting the z-axis of the logical qubit. Therefore this is an effective "bit-flip" channel for one of the logical states (the one defined by an excitation in the shorter-lived cavity).

We quantify this as follows. For each state preparation the populations of the logical state can be expressed as:

| Prep $\|0_\text{L}\rangle$ | Prep $\|1_\text{L}\rangle$ |
|---|---|
| $P_{01} = (1-\epsilon_0)(1-\epsilon_1)$ | $P_{01} = \epsilon_1 \cdot \epsilon_0$ |
| $P_{10} = \epsilon_0 \cdot \epsilon_1$ | $P_{10} = (1-\epsilon_1)(1-\epsilon_0)$ |

where $\epsilon_0$, $\epsilon_1$ are the probabilities of an error in preparing $|0\rangle$ and $|1\rangle$, respectively.

The no-jump backation affects the relative ratio between the population within the logical subspace, and as such we renormalize these population probabilities and define:

$$P'_{01} = \frac{P_{01}}{P_{01} + P_{10}},\ P'_{10} = \frac{P_{10}}{P_{01} + P_{10}}$$

for each of the state preparations.

The functional form of the time evolution of expectation value of the $\hat{\sigma}_z$ is defined in [36], and cast in terms of the notation conventions in this paper takes the form:

$$\langle Z(t)\rangle = \frac{P'_{10} - P'_{10}e^{-(\kappa_A-\kappa_B)t}}{1 - P'_{01}(1 - e^{-(\kappa_A-\kappa_B)t})}$$

where $\kappa_{A(B)} = 1/T_1^{A(B)}$

Under this convention $\langle Z(t)\rangle = +1$ corresponds to $|10\rangle$ and $\langle Z(t)\rangle = -1$ corresponds to $|01\rangle$. With this expression we can extract a time constant corresponding to the lifetime of the qubit to the no-jump evolution for prep $|0_{\mathrm{L}}\rangle$ and $|1_{\mathrm{L}}\rangle$ as:

$$T_{\mathrm{flip}} = \frac{1\mu s}{p(\langle Z(t = 1\mu s)\rangle = +1 \mid \text{prep } 01)},\ T_{\mathrm{flip}} = \frac{1\mu s}{p(\langle Z(t = 1\mu s)\rangle = -1 \mid \text{prep } 10)}$$

For our system's parameters we find that for prep $|0_{\mathrm{L}}\rangle$ and $|1_{\mathrm{L}}\rangle$ the qubit lifetime due to this bit-flip channel is $T_{\mathrm{flip}\ |0_{\mathrm{L}}\rangle\rightarrow|1_{\mathrm{L}}\rangle} = 3.28\ s$ and $T_{\mathrm{flip}\ |1_{\mathrm{L}}\rangle\rightarrow|0_{\mathrm{L}}\rangle} = 4.43\ s$.

*c. Total intrinsic bit-flip*

In order to extract an effective, relevant time-constant ($\mathrm{T}_{\mathrm{flip}}$) representing the intrinsic lifetime of the dual-rail qubit, we look at the error in the nominal duration of a logical gate: 1 $\mu$s. We then define the time-constant as:

$$\mathrm{T}_{\mathrm{flip}} = \frac{1\ \mu\mathrm{s}}{\text{probability of an intrinsic bit-flip at } 1\ \mu\mathrm{s}}$$

where this probability is the sum of the two intrinsic contributions.

As described above, we find that both of these intrinsic bit-flip channels contribute on the order of $\sim 10^{-7}$ at 1 microsecond to the bit-flip probability. As such, for our system's parameters we find that for prep $|0_{\mathrm{L}}\rangle$ and $|1_{\mathrm{L}}\rangle$ the intrinsic qubit lifetime is $\mathbf{T}_{\mathrm{flip}\ |\mathbf{0}_{\mathrm{L}}\rangle\rightarrow|\mathbf{1}_{\mathrm{L}}\rangle} = \mathbf{2.21\ s}$ and $\mathbf{T}_{\mathrm{flip}\ |\mathbf{1}_{\mathrm{L}}\rangle\rightarrow|\mathbf{0}_{\mathrm{L}}\rangle} = \mathbf{2.98\ s}$.